MINI REVIEW

Methane selective oxidation to methanol by metal-exchanged zeolites: a review of active sites and their reactivity†

Muhammad Haris Mahyuddin, [iD] Yoshihito Shiota [iD] and Kazunari Yoshizawa [iD] *

Over the past decade, zeolites (microporous aluminosilicate minerals) have been gaining significant popularity due to their broad applications in catalysis including the dream reaction of selective oxidation (hydroxylation) of methane to methanol at low temperature. In this review, we outline the current main challenges in the development of Fe-, Cu-, Co- and Ni-exchanged zeolites for methane hydroxylation and summarize key findings that have been reported in both spectroscopy and computational studies. Also, using density functional theory (DFT) calculations, we calculate energy diagrams of methane hydroxylation over various structures of metal-oxo active sites in zeolites and discuss some key points that can be improved for achieving higher reactivity. Short outlooks on the future research opportunities are also discussed.
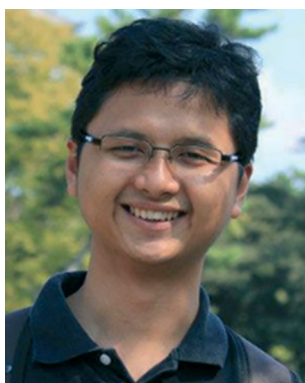
1. Introduction

With declining reserves of crude oil while wind and solar technologies are still in the early stages of development, the utilization of methane becomes more important as a source of clean fossil energy. Methane is an earth-abundant gas contained mainly in natural gas, and it can also be extracted from large

Institute for Materials Chemistry and Engineering and IRCCS, Kyushu University, Fukuoka 819-0395, Japan. E-mail: kazunari@ms.ifoc.kyushu-u.ac.jp
† Electronic supplementary information (ESI) available: All calculated reaction energy diagrams, optimized structures, geometrical parameters, and atomic spin densities. See DOI: 10.1039/c8cy02414f

reserves of shale gas,[1] coalbed methane,[2] and methane hydrate[3] using cost-effective methods. However, since storing and transporting methane over a long distance from remote mining sites to inhabited areas is economically unviable, it is highly desirable to convert methane to condensable chemicals such as methanol on-site. Methanol has enormous potential as both an energy source for hydrogen production[4] and an energy carrier for vehicle fuel or direct methanol fuel cells (DMFCs),[5] as well as for chemical feedstock producing olefins, hydrocarbons, gasoline, *etc.*[6] Unfortunately, the commercially existing technology for such a gas-to-liquid conversion involves a high-cost production of syngas (a mixture of CO and H_2),[7,8] which makes it effective only at large-scale industries. Alternative conversion

Muhammad Haris Mahyuddin received his B.Eng. from Bandung Institute of Technology in Indonesia and M.Eng. from Tohoku University in Japan. After spending two years at Panasonic Corp. Japan as an engineer and another two years at a private university in Indonesia as a lecturer, he started his Ph.D. study on theoretical chemistry in 2015 at Kyushu University under the supervision of Prof. Kazunari Yoshizawa. Having completed the study in 2018, he became a specially appointed assistant professor at the same laboratory.

Muhammad Haris Mahyuddin

Yoshihito Shiota received his bachelor's, master's and Ph.D. degrees from Kyoto University in Japan. He then joined the Institute for Materials Chemistry and Engineering, Kyushu University, as an assistant professor in 2001 and became an associate professor in 2014.

Yoshihito Shiota

routes through oxidative and non-oxidative couplings have also been developed,[8] but their performance in terms of selectivity and productivity is considerably low due to the high temperature required.[9]

Given such backgrounds, a direct, low-cost, and low-temperature chemistry of methane conversion is therefore indispensable and must immediately be available to anticipate the increasing energy demands. Methane hydroxylation (CH_4 + $1/2O_2$ → CH_3OH) is regarded as the most viable way to meet the expectation. The key challenges associated with this process, however, are the cleavage of the strong C–H bonds of methane and the suppression of complete oxidation to CO_2 because methanol has weaker C–H bonds than methane and thus is prone to over-oxidation.

Nature, through a certain kind of enzyme that includes iron or copper centers in its active site (soluble or particulate methane monooxygenase, sMMO or pMMO, respectively), has shown its ability to hydroxylate methane with O_2 under ambient conditions.[10–12] Comparable metal active sites isolated in rigid lattices of zeolite have been developed as synthetic catalysts for methane hydroxylation at low temperature. Taking advantage of its acid sites, a zeolite can be ion-exchanged with metal cations to form metal centers anchored at Al sites on the wall of zeolite micropores. Although a large amount of research has been devoted mainly to iron and copper as the exchanging metal cations,[13–18] other earth-abundant metals such as cobalt, nickel, and zinc still open great opportunities for development. In particular, the low methanol selectivity at high conversion rates of methane is still problematic for the current state of iron- and copper-exchanged zeolites to be implemented industrially.

The oxidizing species on the active sites of metal-exchanged zeolites can be derived from the activation of oxidants such as N_2O, H_2O_2 and ideally O_2. Considering that O_2

cannot directly hydroxylate methane due to the spin-forbidden reaction between the triplet (O_2) and singlet (CH_4) substrates, dioxygen activation therefore becomes very essential in the direct conversion of methane. Specifically, when O_2 is activated on a reduced metal center, the metal facilitates a spin inversion for the triplet O_2, resulting in a metal-superoxo ($M^{n+1}O_2{}^{\cdot-}$), -peroxo ($M^{n+2}O_2{}^{2-}$), or -oxo ($M^{n+4}[O^{2-}]_2$) species that is favorable for the oxidation of singlet alkanes.[8] Very recently, an anaerobic methane hydroxylation by Cu-exchanged zeolites, where water is used as the oxidant instead of O_2 that requires high temperature for activation, was also proposed.[19] The activation of N_2O and H_2O_2 is also important especially for Fe-exchanged zeolites which cannot be activated by O_2. The decomposition of N_2O results in a transfer of the O atom to the Fe center(s) and an irreversible release of N_2 to the atmosphere.[15] The use of N_2O as oxidant, however, faces an insurmountable hurdle associated with its low availability that cannot compete with the large need for industrial-scale methane valorization.[20] This therefore has shifted the challenge from the C–H bond cleavage of methane to the formation of active sites.

Another issue that hampers metal-exchanged zeolites from exhibiting high selectivity is the fact that the formed methanol is difficult to desorb spontaneously from the metal centers but easily over oxidized. Many researchers usually use a solvent such as water and acetonitrile at room or elevated temperature to extract methanol, although this method is not actually preferred because it leads to a dilute methanol solution which requires a high-cost separation.[16] Therefore, the search for metals and oxidants that enable a solvent-free, facile methanol extraction is indispensable. Several strategies have been suggested by Ravi et al.[21] to protect methanol from over-oxidation. One of them is the use of multicomponent catalysts, e.g. Cu-promoted Fe-ZSM-5 zeolite,[22–24] where Fe acts as the active site while Cu acts as a modulator to ensure high methanol selectivity.

Herein, we present a comprehensive yet brief review of the recent progress in methane hydroxylation by Fe-, Cu-, Co- and Ni-exchanged zeolites, extending the previous excellent reviews focusing only on Fe- and Cu-exchanged zeolites.[14–18] Moreover, here we show how mutual interplays between spectroscopy techniques and density functional theory (DFT) calculations have been able to reveal the active site structures, to elucidate the reaction mechanisms, to explore factors influencing the reactivity, and ultimately to find possible solutions for the challenges described above. The rest of this review is organized as follows. Section 2 provides a general introduction to the framework structures of zeolites, nature of acid sites in zeolites, and catalytic performance of metal-exchanged zeolites in the direct conversion of methane to methanol. Sections 3 to 6 summarize the recent experimental and computational findings in the structures, formation, and reactivities of the active sites. Finally, the concluding remarks and the computational methods used for calculating energy diagrams and molecular orbitals presented in this work are provided in sections 7 and 8, respectively.

Kazunari Yoshizawa received his bachelor's, master's and Ph.D. degrees from Kyoto University in Japan under the direction of Prof. Kenichi Fukui and Prof. Tokio Yamabe. After spending one year at Cornell University as a postdoctoral associate in the group of Prof. Roald Hoffmann, he joined Kyoto University, where he became an assistant professor and then associate professor. In 2001, he moved as a full professor to Kyushu University, where his research interests were extended to enzymatic and catalytic reactions as well as electronic properties of molecules and solids. He received the Chemical Society of Japan Award for Creative Work in 2011 and the Japan Society of Coordination Chemistry Contribution Award in 2018.

Kazunari Yoshizawa

2. Metal–exchanged zeolites

2.1 Zeolite frameworks

Zeolites are microporous aluminosilicate materials with channel sizes of molecular dimensions and thus often used as molecular sieves. The primary building units of zeolites are the $[SiO_4]^{4-}$ and $[AlO_4]^{5-}$ tetrahedra (T) which share their O atoms with the neighboring T to form a three-dimensional structure. Different arrangements of how T interlinked to each other lead to 20 secondary building units. These topological subunits can then be combined to form a big variety of zeolite frameworks. According to the zeolite database provided by the International Zeolite Association (IZA),[25,26] there are more than 200 distinct zeolite frameworks available and they are denoted by three capital letters (Table 1). These frameworks can basically be classified according to their pore sizes, i.e. small, medium, and large pores, indicated by the number of T atoms (Si and Al) constructing the channels. For example, SSZ-13 zeolite (CHA framework) is a small-pore zeolite with 8-membered rings (8-MRs) constructing its largest channels (3.8 × 3.8 Å). Although most of the zeolite frameworks have crystal-like ordered structures, some of the structures are partially disordered and/or interrupted (i.e. not all T
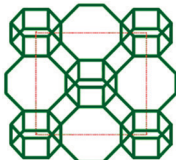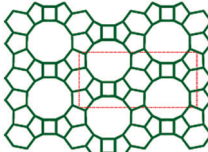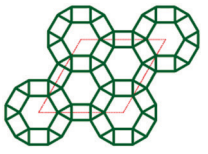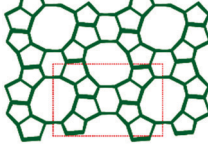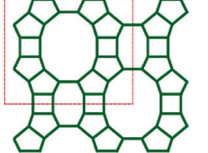
atoms are 4-connected), which are respectively denoted by * and – symbols preceding the three-letter code.

The channel dimensionality of a zeolite can be defined in two different ways: sorption and topological dimensionalities. They correspond to a pore opening larger than 3.4 Å and a pore opening larger than a 6-MR, respectively. Consequently, mordenite (MOR), for example, can have two definitions of channel dimensionality: one- and two-dimensional channel systems, although the former definition is used more often in the literature. The so-called side-pocket windows along the [010] direction of MOR are 8-MRs, but their free diameter is only 3.4 × 4.8 Å.

2.2 Acid sites in zeolites

Acid sites in zeolites are formed as a result of the incorporation of trivalent Al^{3+} into the siliceous zeolite, which results in an excess negative charge that must be compensated for by positively charged cations. Proton (H^+) is one of the most frequently exchanged cations that gives rise to a Brønsted acid site (BAS), where the proton is bonded to the lattice O atom that connects the tetrahedrally coordinated Si^{4+} and Al^{3+} cations. Alternatively, alkaline metal cations such as Na^+

Table 1 Structural information of selected zeolite frameworks retrieved from the zeolite database[25]

IZA code	Material examples	Lattice parameters (Å)	Channel size	Channel dimensionality[b]	Framework image[c]
AEI	SSZ-39 AlPO-18[a]	a = 13.677 b = 12.607 c = 18.497	[100] 3.8 × 3.8 Å [110] 3.8 × 3.8 Å [001] 3.8 × 3.8 Å	Sorption: 3D Topological: 3D	
*BEA	Beta polymorph A	a = 12.632 b = 12.632 c = 26.186	⟨100⟩ 6.6 × 6.7 Å [001] 5.6 × 5.6 Å	Sorption: 3D Topological: 3D	
CHA	SSZ-13 SAPO-34[a]	a = 13.675 b = 13.675 c = 14.767	[001] 3.8 × 3.8 Å	Sorption: 3D Topological: 3D	
MFI	ZSM-5	a = 20.090 b = 19.738 c = 13.142	[100] 5.1 × 5.5 Å [010] 5.3 × 5.6 Å	Sorption: 3D Topological: 3D	
MOR	Mordenite	a = 18.256 b = 20.534 c = 7.542	[001] 6.5 × 7.0 Å [001] 2.6 × 5.7 Å	Sorption: 1D Topological: 2D	

[a] Zeotype consisting of phosphate instead of silica. [b] Sorption and topological channel dimensionalities correspond to a pore opening larger than 3.4 Å and a pore opening larger than a 6-membered ring, respectively. [c] A red rectangle/trapezoid represents the unit cell.

1746 | Catal. Sci. Technol., 2019, 9, 1744–1768

This journal is © The Royal Society of Chemistry 2019

and K^{+} can also be used as the exchange cations. These exchange cations are not covalently bound to the zeolite framework and thus can readily be substituted with a variety of metal cations *via* conventional aqueous ion-exchange methods to form metal centers that are applicable for various catalytic reactions, including NO$_x$ removal from the gas exhaust of automotive engines,[27–29] catalytic cracking,[30,31] methane hydroxylation to methanol, and many others.[32]

The interlinks between the [SiO$_4$][4−] and [AlO$_4$][5−] tetrahedra in zeolites must obey Loewenstein's rule,[33] describing that two Al tetrahedra cannot share one common O atom due to the electrostatic repulsion between the negative charges. This implies that the Al atoms must be separated by at least one Si atom (Al–O–(Si–O)$_n$–Al sequence with $n \geq 1$). Thus, the minimum Si/Al ratio in zeolites is one. The Si/Al ratio is directly related to the acidity (the lower the Si/Al ratio, the higher the acidity)[34] and catalytic activity[35,36] of zeolites.

2.3 Catalytic performance of metal-exchanged zeolites in the hydroxylation of methane

Methane hydroxylation by metal-exchanged zeolites can be achieved through a stepwise (stoichiometric chemical looping) or continuous (catalytic) process, although the former process is more commonly used in experiments due to the higher methanol yield and selectivity. As shown in Fig. 1b, the stepwise process involves three separate steps: (1) activation of the metal–zeolite catalyst by an oxidant at 250–500 °C, (2) methane reaction at 25–200 °C, and (3) methanol extraction using a solvent or steam at 25–200 °C. The main drawback of this process is the high temperature needed for the catalyst activation, which increases the cost. Moreover, the produced methanol cannot desorb on its own and thus needs a solvent-based extraction technique that may lead to a dilute methanol solution. In the continuous process, on the contrary, a gas mixture of O$_2$ or N$_2$O, CH$_4$, and pressurized H$_2$O is reacted with the catalyst at 210–300 °C, producing hydrolyzed methanol without any extraction procedures (Fig. 1a).

Table 2 presents an overview of the performance of Fe-, Cu-, Co- and Ni-exchanged zeolites in methane hydroxylation. The pioneering work was established by Panov and co-workers, who discovered a highly reactive α-oxygen site upon N$_2$O decomposition on Fe-ZSM-5.[37,55,56] This catalyst activates methane at room temperature and produces methanol with 80% selectivity. Besides N$_2$O, a stronger oxidant H$_2$O$_2$ has also been reported to oxidize Fe-ZSM-5 to form active sites that catalyze methane hydroxylation.[22–24] Following this work, Schoonheydt and co-workers reported Cu-ZSM-5 and Cu-MOR zeolites, which activate methane at 125 °C to yield methanol with 98% selectivity.[41,57] A significant number of studies on Cu-exchanged zeolites have been reported, owing particularly to their ability to activate a variety of oxidants including O$_2$, N$_2$O, H$_2$O$_2$,[22] and H$_2$O.[19] Isothermal stepwise[44,50,58] and continuous[45,52] processes of methane hydroxylation by Cu-ZSM-5, Cu-MOR, and Cu-SSZ-13 have also been reported, but the methanol yield and selectivity resulting from these processes are much lower than those from the high-temperature activation, stepwise process. Typically, the produced methanol is extracted off-line, where the reacted catalyst is stirred with a solvent outside the reactor. However, this method makes the process inefficient. Recently, an on-line extraction method, in which steam is introduced directly to the reactor, has also been reported and showed a remarkably high productivity of methanol.[40,46–48,51]

A number of alternative metal cations were also reported as the active sites in zeolites. Beznis *et al.*[53,59] and Krisnandi *et al.*[60] demonstrated that Co-ZSM-5, after activation at 550 °C under O$_2$, is also able to catalyze the direct conversion of methane to methanol at 150 °C, but no further studies have been reported since then. Similarly, there has been a very limited number of reports studying methane hydroxylation by Ni-exchanged zeolites. We noted only Shan *et al.* who reported a successful O$_2$-activated Ni-ZSM-5 for hydroxylating methane below 175 °C.[54] A mononuclear Rh[+] species anchored on ZSM-5 zeolite was also recently reported to be active for methane conversion at 150 °C, yielding 230 μmol of methanol per gram of the catalyst with 60–100% selectivity.[61] This catalyst does not require high-temperature activation with an oxidant. Instead, CH$_4$, O$_2$, and CO are flowed together to the reactor, where CO acts as a co-catalyst that stabilizes the Rh[+] active site. Very recently, Oda *et al.* have reported a mononuclear [Zn[II]–O][+] site in ZSM-5 zeolite that activates methane at room temperature to yield methanol (29 μmol g-cat[−1]) with 94% selectivity.[62] However, a high-cost pretreatment involving H$_2$ is required to form the active site.[62,63]

3. Methane hydroxylation by Fe/ zeolites

3.1 Active site structures

The active site structure of N$_2$O-activated Fe-exchanged zeolites had been debated for nearly three decades since the first
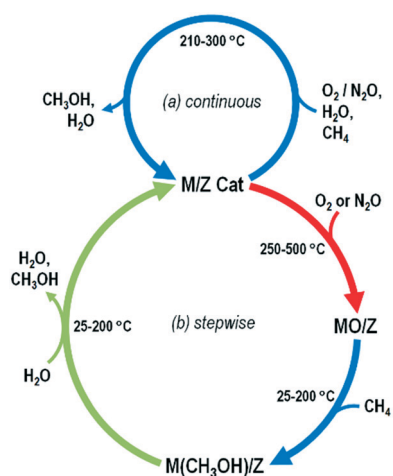

Fig. 1 Schematic representation of (a) continuous and (b) stepwise processes of methane hydroxylation by metal–exchanged zeolite catalysts (M/Z Cat).

This journal is © The Royal Society of Chemistry 2019

Catal. Sci. Technol., 2019, **9**, 1744–1768 | **1747**

Table 2 Selected experimental results of methane hydroxylation by metal-exchanged zeolites

Catalyst	Oxidant	Reaction temp. (°C)	Process[a]	Extracting solvent[b]	Methanol yield (μmol g-cat^{-1})	Productivity (mmol per mol metal)	Methanol selectivity (%)	Ref.
Fe-ZSM-5	N$_2$O	RT	Stepwise	Acetonitrile solution	5.0	—	80	37
	N$_2$O	160	Stepwise	Acetonitrile solution	160	—	76	38
	N$_2$O	25	Stepwise	Ethanol	23	—	94	39
	H$_2$O$_2$	50	Aqueous, continuous	—	22.3	—	17	22
Fe-SSZ-13	N$_2$O	RT	Stepwise	Steam (online)	26.8	681	—	40
Cu/Fe-ZSM-5	H$_2$O$_2$	50	Aqueous, continuous	—	188.8	—	85	22
Cu-ZSM-5	N$_2$O or O$_2$	175	Stepwise	Acetonitrile solution	8.2	—	98	41
	N$_2$O or O$_2$	RT	Stepwise	Acetonitrile solution	0.81	—	—	41
	H$_2$O$_2$	50	Aqueous, continuous	—	65.3	—	83	22
	O$_2$	200	Stepwise	Steam	16.0	30	—	42
	O$_2$	200	Stepwise	Water	9.0	14.3	—	43
	NO	150	Isothermal stepwise	Steam	0.6	—	—	44
	O$_2$	210	Continuous	—	1.81 (1 h)	5.2	71	45
Cu-MOR	N$_2$O or O$_2$	175	Stepwise	Acetonitrile solution	11.3	—	—	41
	O$_2$	200	Stepwise	Steam	31.0	40	—	42
	O$_2$	200	Stepwise	Water	31.2	48.3	—	43
	O$_2$	150	Stepwise	Steam (online)	67	<250	—	46
	O$_2$	200	Stepwise	Steam (online)	160	—	80[c]	47
	O$_2$	200	Stepwise	Steam (online)	170	470	90	48
	O$_2$	200	Stepwise	Water	118.5	180	95	49
	O$_2$	200	Isothermal stepwise	Steam	56.2 (37 bar CH$_4$)	—	—	50
	N$_2$O	150	Stepwise	Steam (online)	97	>300	—	46
	H$_2$O	200	Stepwise	Steam (online)	—	204	97	19
Cu-SSZ-13	O$_2$	200	Stepwise	Steam	31.0	60	—	42
	O$_2$	200	Stepwise	Water	30.0	42.4	—	43
	O$_2$	200	Stepwise	Steam (online)	125.0	200	—	51
	N$_2$O	260	Continuous	—	19 (1 h)	—	27	52
Cu-SSZ-16	O$_2$	200	Stepwise	Steam	39.0	50	—	42
Cu-SSZ-39	O$_2$	200	Stepwise	Steam	36.0	90	—	42
Cu-Omega	O$_2$	200	Stepwise	Water	86.1	92.8	—	43
Co-ZSM-5	O$_2$	150	Stepwise	Ethanol	0.3–0.4	—	40–100	53
Ni-ZSM-5	O$_2$	175	Stepwise	Water	5.1	—	—	54

[a] All reactions are in the gas phase unless otherwise stated. [b] The extraction methods are mostly off-line, unless otherwise stated in the parentheses. [c] Selectivity of both methanol and dimethyl ether, the latter of which is derived from the condensation of two methanol molecules (2CH$_3$OH → CH$_3$OCH$_3$ + H$_2$O).

studies of methane-to-methanol[55] and benzene-to-phenol[64] conversions by Fe-ZSM-5 were reported by Panov *et al.* in the 1990s. A mononuclear FeO$^+$ active site was first predicted theoretically to catalyze these reactions,[65] but then the discovery of a bis(μ-oxo)diiron active site in sMMO led researchers to suggest the same active site in Fe-ZSM-5.[66–70] A mononuclear OFeO core in ZSM-5 zeolite[71,72] and two Fe^{II} cations on two adjacent six-membered rings (6-MRs) of ferrite zeolite were also proposed as the active site.[73,74] Despite such great research efforts, conclusive evidence for the actual active site structure was reported only recently.[75,76] This was due to the difficulty in distinguishing the true active iron center from the inactive spectator iron centers.

Utilizing two spectroscopy methods, namely diffuse reflectance ultraviolet-visible (DR-UV-vis) and site-selective mag-

netic circular dichroism (MCD), Snyder *et al.*[75] successfully identified a mononuclear square-planar Fe center, which was previously characterized by Panov and co-workers as an α-Fe^{II} site,[38,77,78] on an Al pair site of the β-type 6-MR of *BEA zeolite. Specifically, the authors observed from the DR-UV-vis spectra an intense band at 40 000 cm^{-1} and three weak bands at 15 900, 9000, and 5000 cm^{-1} for the inactivated Fe-*BEA (Fig. 2a).[75] After N$_2$O activation at 250 °C, only the 15 900 cm^{-1} absorption band shifts to 16 900 cm^{-1} with a slight increase of intensity (Fig. 2b, red line), suggesting that the 15 900 cm^{-1} band formed before the activation corresponds to the α-Fe^{II} while the 16 900 cm^{-1} band formed after the activation corresponds to an α-O which forms a (Fe^{IV}=O)$_\alpha$ active site. It is further seen from the DR-UV-vis spectra of the CH$_4$-reacted Fe-*BEA that the 16 900 cm^{-1} band disappears after

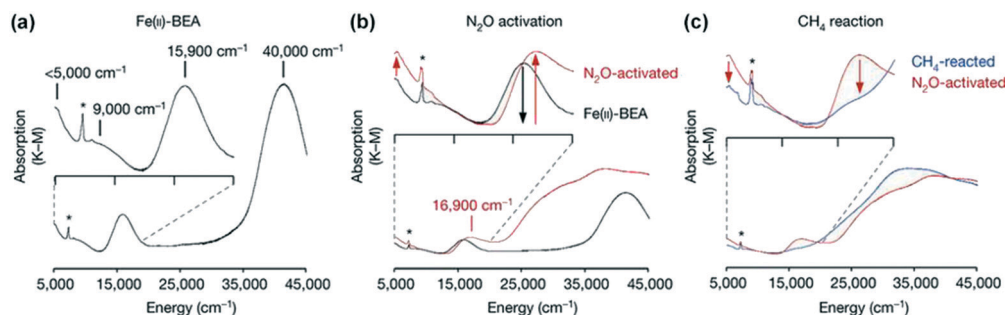**Fig. 2** DR-UV-vis spectra of Fe-*BEA (a) before activation, (b) after N_2O activation at 250 °C, and (c) after reaction with methane at room temperature. Adapted with permission from ref. 75. Copyright 2016 Nature Publishing Group.

the reaction at room temperature (Fig. 2c, blue line), indicating the formation of oxygenated products such as methanol $CH_3(O_\alpha)H$.

Furthermore, as shown in Fig. 3a, the MCD spectra show a band at $15\,100$ cm^{-1} that is correlated to the $15\,900$ cm^{-1} absorption band of the DR-UV-vis (α-Fe^{II} site) and sensitive to magnetic field and temperature. Varying the magnetic field from 1.5 to 7.0 Tesla increases the intensity of the MCD $15\,100$ cm^{-1} band, suggesting that the α-Fe^{II} is paramagnetic and different from the antiferromagnetic Fe^{II}–O–Fe^{II} and Fe^{II}–OH–Fe^{II} structures previously proposed as the active site.[70,77] This confirms that the active site is a mononuclear (Fe^{IV}=O)$_\alpha$. Moreover, the high energy DR-UV-vis spectra at $15\,900$ cm^{-1} implies that the α-Fe^{II} site is unlikely to have an octahedral, tetrahedral, or trigonal bipyramidal geometry. Instead, the Hamiltonian and Mössbauer parameters show that the α-Fe^{II} site has a square planar geometry (Fig. 3b, left) with the quintet ground state (spin quantum number, $S = 4/2$). Fig. 3b (right) shows a square pyramidal (Fe^{IV}=O)$_\alpha$ active site formed after N_2O activation over the α-Fe^{II} site sit-

ting on two Al lattices within the β-type 6-MR of *BEA zeolite, as also suggested on the 6-MRs of MFI, FER, and CHA zeolite frameworks.[79,40] However, the (Fe^{IV}=O)$_\alpha$ species has a resonance structure of (Fe^{III}–O$^{\cdot-}$)$_\alpha$ and it is difficult to determine which of the two electronic structures is the ground state (see section 3.2 for details).

A different approach in methane hydroxylation by Fe-exchanged zeolites was reported by Hutchings and coworkers, who carried out the reaction in the liquid phase using H_2O_2 as an oxidant and in the presence of Cu^{2+}, Al^{3+}, or Ga^{3+} cations that promote the selectivity toward methanol.[22–24] The XANES and EXAFS measurements reported in ref. 22, however, proposed an active site that involves an antiferromagnetically coupled high-spin octahedral dinuclear Fe^{III}, instead of the mononuclear α-Fe^{II} site. Using DFT calculations, the authors then obtained that a [Fe$_2$(μ_2-OH)$_2$(OH)$_2$(H_2O)$_2$]$^{2+}$ complex well matches the EXAFS data. In the absence of cationic promotion, this active species activates methane with a measured activation energy of 14.6 kcal mol^{-1}, in good agreement with a DFT-calculated value of 12.0 kcal mol^{-1}, but with a methanol selectivity of only 19%.[22] Only after the Cu^{2+} promotion is the methanol selectivity increased significantly to 83%, although the total amount of oxygenated products is insignificantly improved, suggesting that Cu^{2+} acts only as a promoter but does not involve directly in the reaction. Therefore, as observed from EPR spectroscopy, such an increase in methanol selectivity is primarily due to a concentration decrease in hydroxyl radicals, which can lead to the formation of CH_3OOH and $HCOOH$ side products.
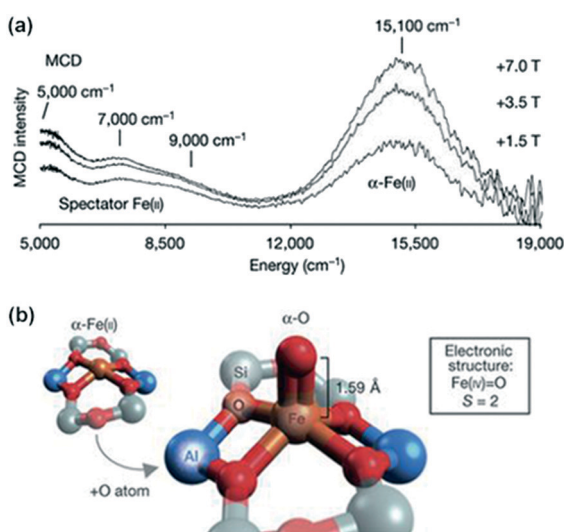

Fig. 3 (a) MCD spectra of Fe-*BEA before N_2O activation. (b) DFT-predicted structure of the (Fe^{IV}=O)$_\alpha$ active site in Fe-*BEA zeolite. Adapted with permission from ref. 75. Copyright 2016 Nature Publishing Group.

3.2 N_2O activation

As Fe-exchanged zeolites are known to be unreactive toward O_2,[80,81] the discovery of mononuclear the α-Fe^{II} site in zeolites confirms that only oxidants whose O atoms are weakly bonded with two electrons needed for a cleavage can activate the α-Fe^{II} to (Fe^{IV}=O)$_\alpha$. One of these oxidants is N_2O with a bond dissociation energy of only 42 kcal mol^{-1}. As we previously reported,[82] in N_2O activation over Fe^{II}-ZSM-5, the molecule is decomposed into N_2 released to the atmosphere and an O ligand bound to the α-Fe^{II} center. In Fig. 4, we

recalculate our previous DFT results[82] by adding dispersion (van der Waals) corrections and predict that the Fe[II]-ZSM-5 prefers the quintet high-spin state ($S = 4/2$) rather than the triplet low-spin state ($S = 2/2$). The N_2O molecule is initially adsorbed on the Fe[II] center with a rather strong adsorption energy of -7.3 kcal mol^{−1} and a short Fe···O distance of 2.263 Å. Then, the N–O bond is cleaved *via* a transition state (**TS**) with a separated N···O distance of 1.468 Å and an activation energy of 13.7 kcal mol^{−1}, which confirms the previous DFT results without dispersion correction (15.1 or 16.5 kcal mol^{−1})[82,83] and agrees very well with the experimental value (14.1 kcal mol^{−1}).[84]

Dubkov *et al.*[77] and Pirngruber *et al.*[85,86] interpreted from their respective Mössbauer spectra and resonance inelastic X-ray scattering that the formed $[FeO]^{2+}$ active site favors the $(Fe^{III}–O^{·-})_{\alpha}$ electronic structure. However, recent experimental results suggested the preference for the $(Fe^{IV}=O)_{\alpha}$ electronic structure,[75] which confirms the previous DFT prediction.[87] In Table 3, we list the atomic spin densities of α-Fe and α-O atoms in $[FeO]^{2+}$-ZSM-5, which were calculated by using different DFT methods. The α-Fe and α-O atoms having spin densities of 3 and 1, respectively, suggests that the ground state is the $(Fe^{III}–O^{·-})_{\alpha}$, while those of 4 and 0, respectively, suggest otherwise, *i.e.* $(Fe^{IV}=O)_{\alpha}$. However, the table shows non-integer values of spin densities since the orbitals are not purely Fe-3d or O-2p, but are strong mixtures.[88] The values range from 3.10 to 3.55 for the α-Fe and from 0.14 to 0.51 for the α-O, depending on the type of functional used in the calculations. Thus, it is difficult for DFT calculations to decide which one is the ground-state electronic structure. Nonetheless, the PBE+U, meta-GGA MS1, and HSE06 hybrid methods, which are considered relatively accurate, tend to predict the $(Fe^{IV}=O)_{\alpha}$ as the ground state.
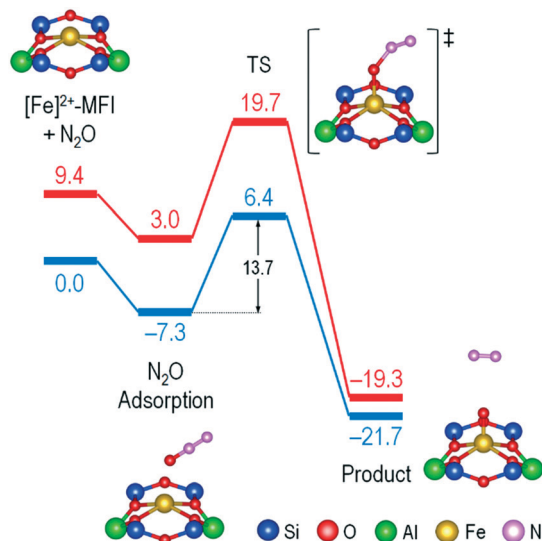

Fig. 4 DFT(PBE)-calculated energy diagrams of N_2O decomposition over α-Fe[II] hosted on the T11/T11 Al pair site of the δ-type 6-MR of ZSM-5 (MFI) zeolite. Blue and red lines correspond to the quintet high-spin and triplet low-spin states, respectively. Energies are given in kcal mol^{−1} and include the vdW-D2 dispersive correction.

3.3 Reactivity of various Fe/O active site motifs

Scheme 1 shows one of the possible reaction mechanisms for methane hydroxylation by $[FeO]^{2+}$-exchanged zeolites, namely homolytic H-atom abstraction (HAA) or rebound mechanism. In this mechanism, methane is initially adsorbed on the active site (left); then one H atom of methane is abstracted in a homolytic manner through a radical-like transition state to form a methyl radical (middle), and finally a methanol molecule is formed through a direct $HO–CH_3$ rebound step (right).[90] Alternatively, a C–H bond of methane can be cleaved in a heterolytic manner *via* a four-center transition state (see Scheme S1†) which leads to the formation of a methyl ligand bound to the Fe center and to the subsequent formation of methanol *via* a $Fe–CH_3$ cleavage and a $HO–CH_3$ rebound.[65,91] This is often referred to as a non-radical or heterolytic HAA mechanism. More comprehensive overviews of these two reaction mechanisms as well as the Fenton-type mechanism can be found elsewhere.[92,93]

We previously reported the hydroxylation of methane over $[FeO]^{2+}$ in the gas phase[94,95] and in the periodic structure of ZSM-5 zeolite.[82] In Fig. 5, we recalculate our previous energy diagrams[82] of the homolytic HAA of methane by $[FeO]^{2+}$-ZSM-5 by adding the dispersive correction, which is important for reasonably calculating the methane adsorption and methanol desorption energies. Initially, methane is adsorbed on the active site with a bent Fe–O–CH_4 geometry, due to a compromise position between two orbital overlaps (*i.e.* O-2p_x···CH_4-σ and O-2p_z···CH_4-σ overlaps).[82,87] The adsorption energy is calculated to be -6.3 kcal mol^{−1} with a C···O distance of 3.589 Å. Subsequently, one C–H bond of methane is cleaved in a homolytic manner with a separation C···H distance of 1.234 Å and an activation barrier of 7.0 kcal mol^{−1}. The latter value is in good agreement with that for $[FeO]^{2+}$-SSZ-13 (6.0 kcal mol^{−1}),[90] suggesting that a change in the zeolite structure insignificantly affects the reactivity of $[FeO]^{2+}$-zeolites. The resultant radical intermediate is predicted by PBE functional to be less stable than the methane adsorption, but the B3LYP and HSE03 hybrid functionals tend to predict otherwise.[75,96]

The methyl radical is then recombined directly with the OH moiety to form a methanol molecule bound to the Fe center. This process requires a negligible activation energy of only 3.3 kcal mol^{−1}. The formed methanol is very stable with an insignificantly elongated Fe–O bond length (2.041 Å, Table S5†). The desorption of methanol from the Fe center requires a high desorption energy of 32.8 kcal mol^{−1}, which is by 25.8 and 19.1 kcal mol^{−1} higher than the methane's C–H bond and O–N_2 bond activation barriers, respectively. This suggests that methanol desorption is the rate-determining step. The overall reaction takes place in the quintet high-spin state and is exothermic by -8.2 kcal mol^{−1}.

In Table 4, we summarize DFT-calculated methane C–H bond activation barriers and methanol desorption energies, which have been reported so far for various Fe/O active site motifs in zeolites. As shown in this table, the mononuclear $[FeO]^+$ and $[FeO]^{2+}$ species activate methane with activation

1750 | *Catal. Sci. Technol.*, 2019, **9**, 1744–1768

This journal is © The Royal Society of Chemistry 2019

Table 3 DFT-calculated Fe–O bond length as well as α-Fe and α-O atomic spin densities (ρ) of [FeO]$^{2+}$-ZSM-5 in the high-spin quintet state (S = 4/2)

Zeolite framework	Computational method[a]	Fe–O (Å)	ρ (α-Fe)	ρ (α-O)	Ref.
MFI (δ site)	P/PBE-D2	1.617	3.10	0.51	82
MFI (δ site)	P/PBE+U-D2[b]	1.618	3.48	0.26	This work
MFI (δ site)	P/MS1-D2	1.633	3.47	0.21	This work
MFI (δ site)	C/HSE06	1.611	3.55	0.14	This work
MFI (α site)	C/B3LYP	1.589	3.30	0.43	87

[a] Structure/functional-dispersion correction; C and P stand for cluster model and periodic structure, respectively. [b] U = 4.0 eV for Fe, as suggested by Wang *et al.*[89]

Scheme 1 Proposed reaction mechanism of methane hydroxylation by [FeO]$^{2+}$-exchanged zeolites *via* a homolytic H-atom abstraction leading to the formation of a methyl radical and a subsequent methanol molecule. Adapted with permission from ref. 90. Copyright 2016 American Chemical Society.

barriers of less than 20 kcal mol^{-1}. However, considering that Fe-zeolites can activate methane even at room temperature while Cu-zeolites require at least 125 °C (see section 4), the methane activation barrier required by Fe-zeolites should be lower than that required by Cu-zeolites (11–16 kcal mol^{-1}). In this sense, the [FeO]$^{2+}$ species therefore best represents the active site in Fe-zeolites. As discussed above, the [FeO]$^{2+}$ active site requires a methanol desorption energy that is three times higher than that of the C–H activation of methane.

Fig. 5 DFT(PBE)-calculated energy diagrams of methane hydroxylation by [FeO]$^{2+}$ hosted on the T11/T11 Al pair site of the δ-type 6-MR of ZSM-5 zeolite. Energies are given in kcal mol^{-1} and include the vdW-D2 dispersive correction.

This explains why the formed methanol cannot desorb on its own and thus requires extraction procedures.

Recently, Snyder *et al.*[76] reported a comparison of O–H bond formation energies ($\Delta E_{O–H}$) and intrinsic C–H bond activation barriers of methane ($E_{a,int}$) between several geometries of mononuclear Fe–O species found in zeolites, biuret-modified tetraamido macrocyclic ligand (bTAML), pentadentate pyridine (N$_4$Py), and tetramethylguanidino (TMG$_3$-tren). These complexes have geometries of pyramidal, pyramidal, octahedral, and trigonal bipyramidal, respectively. As shown in Table 5, the $\Delta E_{O–H}$ in FeO/zeolites (-102 kcal mol^{-1}) is the strongest one even when compared to that in FeO/bTAML which has the same geometry but different coordinated elements and ground state. Such a strong O–H bond drives the methane activation to proceed with a low activation energy (5.3 kcal mol^{-1}), which is more than half of that for other FeO complexes. The authors suggested several structural features that impart such a remarkable reactivity: (1) a vacant *trans* axial position which provides a large driving force for the O–H bond formation, (2) a moderately weak equatorial ligand field (see also ref. 100) leading to a high spin ground state, and (3) the presence of zeolite lattice constraints which enforce an unstable but reactive combination of (1) and (2).
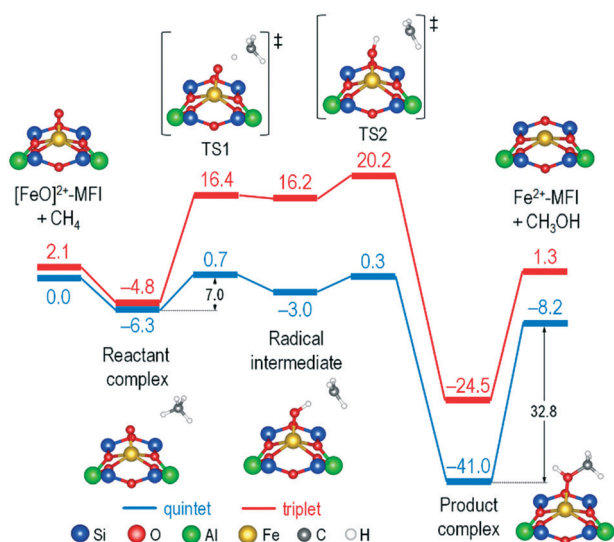
4. Methane hydroxylation by Cu/zeolites

4.1 Active site structures
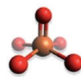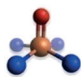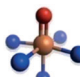
On the basis of UV-vis spectra observation of the 22 700 cm^{-1} absorption band, the active site in the N$_2$O- and O$_2$-activated Cu-ZSM-5 was initially thought to be a bis(μ-oxo)dicopper

This journal is © The Royal Society of Chemistry 2019

Catal. Sci. Technol., 2019, **9**, 1744–1768 | **1751**

Table 4 DFT-calculated methane activation barriers and methanol desorption energies reported so far for methane hydroxylation by various Fe/O active site motifs in zeolites

Active site motif	Zeolite framework	Al site(s)	Computational method[a]	C–H cleavage mechanism	C–H activation barrier (kcal mol⁻¹)	MeOH desorption energy (kcal mol⁻¹)	Ref.
$[FeO]^+$	MFI	—	C/B3LYP	Heterolytic	16.0	26.4	65
	MFI	10MR(T1)	P/PBE-D2	Heterolytic	12.3	35.9	91
$[FeO]^{2+}$	*BEA	β-6MR(T6/T6)	C/B3LYP	Homolytic	3.6	—	75
	MFI	α-6MR(T1/T7)	C/B3LYP	Homolytic	6.6^b	23.8	87
	MFI	δ-6MR(T11/T11)	P/PBE-D2	Homolytic	7.0	32.8^c	82
	AEI	6MR(T1/T2)	P/PBE-D2	Homolytic	7.5	25.2^c	82
	CHA	6MR(T1/T1)	P/PBE-D2	Homolytic	6.0	—	90
$[Fe_2(\mu\text{-O})]^{2+}$	MFI	5MR(T9/T12)	C/B3LYP	Homolytic	26.3^b	—	97
	MFI	5MR(T9/T12)	C/B3LYP	Homolytic	40.5	9.5	98
	MFI	—	C/PBE	Heterolytic	31.6	34.6	99
$[Fe_2(\mu\text{-O})_2]^{2+}$	MFI	5MR(T9/T12)	C/B3LYP	Homolytic	41.5	8.9	98
$[Fe_2(\mu\text{-OH})_2]^{2+}$	MFI	—	P/PBE+U	Homolytic	12.0	—	22
$[Fe_2(\mu\text{-O})(\mu\text{-OH})]^{2+}$	MFI	5MR(T9/T12)	C/B3LYP	Homolytic	34.0	—	98
$[HOFe_2(\mu\text{-O})]^{2+}$	MFI	5MR(T9/T12)	C/B3LYP	Homolytic	20.2	10.7	98

[a] Structure/functional-dispersion correction; C and P stand for cluster model and periodic structure, respectively. [b] Apparent activation barrier measured from the initial structure (Fe/O)Z + CH_4, no formation of reactant complex. [c] Recalculated data including the vdW-D2 dispersion correction.

Table 5 DFT-calculated OH bond formation energy (ΔE_{O-H}, kcal mol⁻¹) and intrinsic activation energy of methane ($E_{a,int}$, kcal mol⁻¹) for different geometries of $[FeO]^{2+}$ in zeolites, bTAML, N_4Py, and TMG_3tren. Adapted with permission from ref. 76. Copyright 2018 National Academy of Science

	Zeolites	bTAML	N_4Py	TMG_3tren
Geometry	Pyramidal	Pyramidal	Octahedral	Trigonal bipyramidal
Spin (S)	4/2	2/2	2/2	4/2
ΔE_{O-H}	−102	−75	−80	−79
$E_{a,int}$	5.3	15.1	12.3	12.0

$[Cu_2^{III}(\mu\text{-O})_2]^{2+}$,[41,57] but it was then revised to a mono(μ-oxo)dicopper $[Cu_2^{II}(\mu\text{-O})]^{2+}$ based on the observation of resonance Raman (rR) spectra[101] showing the absence of vibrations at 600 and 1100 cm⁻¹ (see Fig. 6a), which are the characteristics of bis(μ-oxo) and superoxo species, respectively. Moreover, with the absence of an O–O bond in the structure, which excludes any peroxo and hydroperoxo species from the candidacy for the active site, the observed peaks at 456, 870, and 1725 cm⁻¹ shown in Fig. 6a are thus assigned respectively to the symmetric stretch, antisymmetric stretch, and second quantum antisymmetric stretch of $Cu_2(\mu\text{-O})$ species previously known in a $Fe_2(\mu\text{-O})$ complex.[102] Fig. 6b shows that the $[Cu_2(\mu\text{-O})]^{2+}$ active species is hosted on a pair of Al atoms separated by two Si atoms within the 10-MR channel of ZSM-5 zeolite with a wide Cu–O–Cu angle of 140°.[101] The bridging O atom is highly reactive and responsible for cleaving the strong C–H bond of methane with a low activation barrier (E_a = 15.7 ± 0.5 kcal mol⁻¹, from an Arrhenius plot).[101] The same mono(μ-oxo)Cu_2^{II} active site has also been proposed for pMMO,[21,103] whereas the bis(μ-oxo)Cu_2^{III} in the closed-shell singlet[104,105] and triplet[106] states was predicted by DFT calculations to be low and high, respectively, in reactivity toward methane.

Similarly, Vanelderen et al. observed the formation of a 22 200 cm⁻¹ absorption band from UV-vis characterization on Cu-MOR zeolite after O_2 activation at 250 °C.[107] Raising the temperature to 450 °C after the activation, the authors further observed two distinct absorption maxima contributing to the 22 200 cm⁻¹ band, one of which (21 900 cm⁻¹) is unstable above 330 °C, while the other one (23 100 cm⁻¹) persists in O_2 above 330 °C. The rR spectra of the activated Cu-MOR show good resemblances with those for the activated Cu-ZSM-5 (Fig. 7a), suggesting that the two observed absorption maxima correspond to two distinct $[Cu_2(\mu\text{-O})]^{2+}$ active sites, where the normal coordinate analysis and Eyring plots identify them to be similar in geometry (∠CuOCu = 137° and 141°) but different in reactivity toward methane (E_a = 14.7 ± 0.5 and 11.1 ± 0.5 kcal mol⁻¹).[107] A recent report by Pappas et al.[48] also revealed that the active site nuclearity in Cu-MOR is a dicopper, following the Cu K-edge XANES and XAS investigations by van Bokhoven and co-workers, who suggested a two-electron CH_4 conversion mechanism based on the Cu^{II}/Cu^I redox couple rather than on the Cu^{III}/Cu^{II} one (e.g. $[Cu_2^{III}(\mu\text{-O})_2]^{2+}$ reduced to $[Cu_2^{II}(\mu\text{-O})]^{2+}$), or alternative routes involving Cu^{II}–O˙ radicals.[108,109]

1752 | Catal. Sci. Technol., 2019, 9, 1744–1768
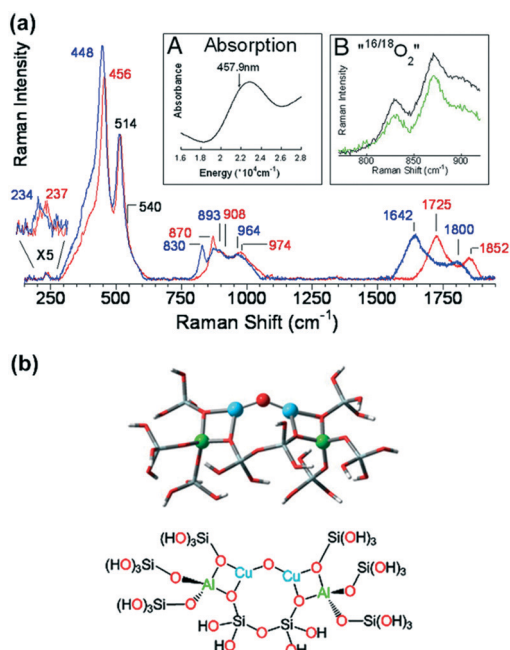
This journal is © The Royal Society of Chemistry 2019

Fig. 6 (a) Resonance Raman (rR) spectra of Cu-ZSM-5 zeolite after activation by $^{16}O_2$ (red) and $^{18}O_2$ (blue). (b) Proposed $[Cu_2(\mu\text{-}O)]^{2+}$ active species hosted on the 10-MR channel of ZSM-5 zeolite, where the Al pair is separated by two Si atoms. Adapted with permission from ref. 101. Copyright 2009 National Academy of Science.
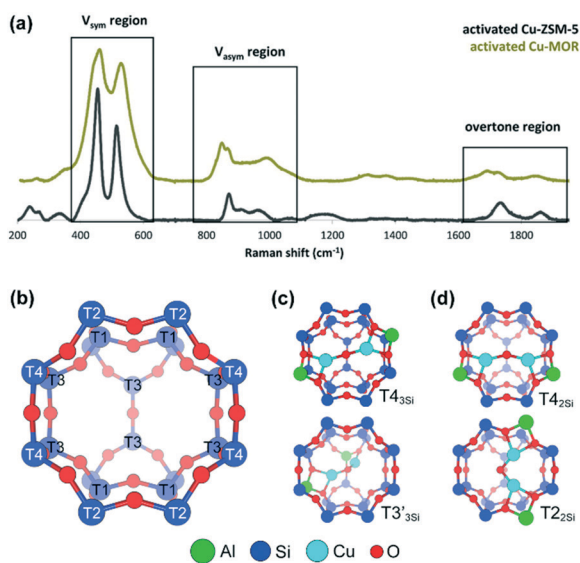

Fig. 7 (a) rR spectra of O_2-activated Cu-ZSM-5 and Cu-MOR. Adapted with permission from ref. 107. Copyright 2015 American Chemical Society. (b) 8-MR side-pocket windows in MOR. A $[Cu_2(\mu\text{-}O)]^{2+}$ active species hosted on different Al pair sites separated by (c) 3 or (d) 2 Si atoms within the 8-MR side pockets.

Recently, Snyder et al. suggested from rR spectra combined with cluster-modelled DFT calculation that the two $[Cu_2(\mu\text{-}O)]^{2+}$ active species are hosted on the T4/T4 and T3/T3 Al pair sites of MOR with three Si atoms separating the Al pair (respectively referred to as $T4_{3Si}$ and $T3'_{3Si}$ in Fig. 7c, where the prime (′)

symbol indicates that the two Al atoms are located at different zeolite rings). Theoretically, an activation barrier can be calculated from the adsorbed and non-adsorbed states of the molecule, resulting in two different values referred to as true and apparent activation barriers, respectively. From the calculated apparent activation barriers, they concluded that the lower methane activation enthalpy is attributed to a more constricted region of $T3'_{3Si}$ in the 8-MR side pocket of MOR.[110] However, as shown in Fig. S1,† our DFT computational results using the periodic structure of MOR show that both the true and the apparent activation barriers for the HAA of methane over the $T3'_{3Si}$ active site (19.9 and 8.6 kcal mol^{-1}, respectively) are higher than those over the $T4_{3Si}$ active site (13.2 and 8.0 kcal mol^{-1}, respectively). This suggests that the constricted space around the $T3'_{3Si}$ site does not affect the reactivity. Instead, it influences the adsorption energy of methane on the $T3'_{3Si}$ active site (−11.3 kcal mol^{-1}), which is twice stronger than that on the $T4_{3Si}$ active site (−5.2 kcal mol^{-1}) due to higher van der Waals forces.

In contrast to the above work by Snyder et al.,[110] we previously reported a DFT study of methane hydroxylation over the $[Cu_2(\mu\text{-}O)]^{2+}$ active site hosted on the $T2_{2Si}$ and $T4_{2Si}$ Al pair sites, with two Si atoms separating the Al pair (Fig. 7d).[111] We found that the C–H activation energies (14.4 and 10.9 kcal mol^{-1}) agree very well with the experimental values[107] and suggested that the lower methane activation enthalpy is attributed to the smaller Cu–O–Cu angle of the $[Cu_2(\mu\text{-}O)]^{2+}$ active site formed on the $T2_{2Si}$ site. This angle is correlated to the repulsive antibonding interaction between the acceptor orbital of $[Cu_2(\mu\text{-}O)]^{2+}$-zeolite and the donor orbital of methane, where a small ∠CuOCu leads to a stronger repulsion that results in an earlier transition state (see section 4.4 for details).[112]

In addition to the medium-pore Cu-ZSM-5 and large-pore Cu-MOR zeolites, the $[Cu_2(\mu\text{-}O)]^{2+}$ species has also been proposed as the active site in the small-pore Cu-SSZ-13 (CHA), where a trans-μ-1,2-peroxo dicopper also coexists as the active site, as observed from rR spectra at 360, 510, 580, 617, and 837 cm^{-1} for O_2-activated Cu-SSZ-13 (Fig. 8).[113] While the 617 cm^{-1} band corresponds to the symmetric stretch of the $[Cu_2(\mu\text{-}O)]^{2+}$ species, the other four bands correspond to the vibrations of the trans-μ-1,2-peroxo-Cu_2. A recent UV-vis-NIR analysis by Oord et al., however, does not show any evidence for the formation of $[Cu_2(\mu\text{-}O)]^{2+}$.[114] Nonetheless, we previously predicted that a $[Cu_2(\mu\text{-}O)]^{2+}$ active site in the 8-MR of the CHA framework has a ∠CuOCu of 94° and abstracts an H atom of methane with an activation energy of 11.4 kcal mol^{-1}.[112]

In contrast, Kulkarni et al. theoretically suggested $[CuOH]^+$ as the active site in methane hydroxylation by Cu-SSZ-13,[115] following the spectroscopy leads reported by Lamberti and co-workers for NO_x decomposition.[116,117] However, Pappas et al.[51] recently reported that the $[CuOH]^+$ is not directly involved in the reaction due to its self-reductive nature, but behaves only as a precursor to form the active site. Despite the disagreement, Sushkevich et al.[118] recently suggested that two interacting $[CuOH]^+$ species in MOR could act as a

This journal is © The Royal Society of Chemistry 2019
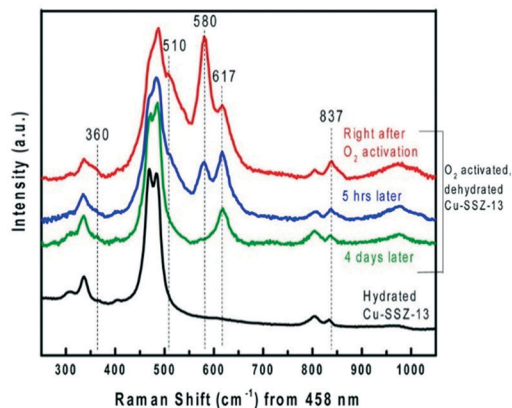
Catal. Sci. Technol., 2019, 9, 1744–1768 | 1753

Fig. 8 rR spectra of Cu-SSZ-13 zeolite after O_2 activation. Adapted with permission from ref. 113. Copyright 2017 American Chemical Society.

plausible active species. The [CuOH]$^+$ species was first identified from FTIR, XAS and XES spectroscopy of Cu-SSZ-13 dehydrated at 250 °C in an O_2-rich environment[117] after confirming the absence of the [Cu$_2$(μ-O)]$^{2+}$ signature peaks in the UV-vis spectra.[119] As shown in Fig. 9 (red curve), in the FTIR spectra of an O_2-activated Cu-SSZ-13 there are two spectra at 3656 and 905 cm^{-1}, which are the [CuOH]$^+$ fingerprints.[116,117] These two spectra are unobserved in the He-activated Cu-SSZ-13 and H-SSZ-13 (Fig. 9, black and grey curves, respectively), suggesting that the [CuOH]$^+$ species only appear upon an oxidative thermal treatment of the Cu-SSZ-13 catalyst; otherwise they undergo a self-reduction to bare Cu$^+$ ions as a consequence of OH extra-ligand loss. The [CuOH]$^+$ species has been suggested to be preferentially hosted on an Al site within the 8-MR of the CHA zeolite framework.[117]

In recent years, trinuclear copper active species have aroused increasing interest. Grundner et al.,[47] who proposed the [Cu$_3$(μ-O)$_3$]$^{2+}$ active site in Cu-MOR zeolite, observed an exchange stoichiometry of 2/3 when the Brønsted acid sites (H$^+$) in H-MOR are substituted by Cu^{2+} ions (a slope of 0.69
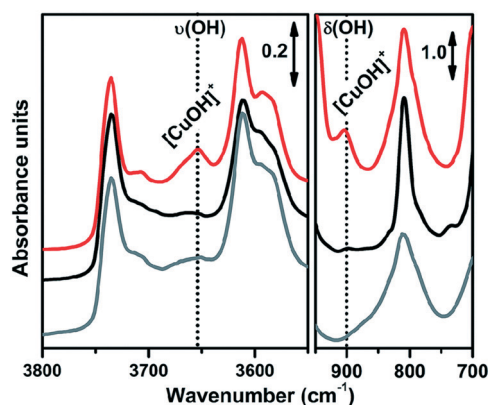

Fig. 9 FTIR spectra of the O_2-activated Cu-SSZ-13 zeolite (red). The spectra of He-activated Cu-SSZ-13 (black) and H-SSZ-13 (grey) are also shown for comparison. Adapted from ref. 117 published by The Royal Society of Chemistry.

in Fig. 10a, black line), indicating that two lattice Al ions originally having the protons are now hosting three Cu cations. The trinuclear Cu-oxo active species is obtained after activating the Cu-MOR catalyst under O_2 environment at 450 °C. Fig. 10a (red line) and b show slopes of 0.31 and 0.33, respectively, indicating that three Cu centers are involved in the oxidation of one methane molecule. By finding a good fit between DFT-predicted structure and experimental EXAFS data for the activated Cu-MOR, the authors concluded that the active site has a structure of [Cu$_3$(μ-O)$_3$]$^{2+}$ and sits on the T2/T2 Al pair site of the 8-MR side pocket of MOR (Fig. 10c and d).[120] In a separate report,[120] the authors elucidated that the use of Na-form zeolites, instead of the H-form zeolites, forms co-cations competing for the exchange positions preferred by the Cu^{2+} centers and thus leads to a heterogeneous speciation of Cu such as dimers and monomers.

The possibility of forming larger clusters of Cu active site has also been discussed theoretically based on the thermodynamic stability.[121,122] Palagin et al.[122] suggested that the stability generally increases with the cluster size due to an additional stabilizing effect of the multiple Cu–O linkages. Paolucci et al. further explained that such multicopper clusters are possible with the probability greatly increased by the potential effects of dynamic structural behavior,[123,124] but might be restrictive only for Cu-zeolites with high Si/Al ratios.

4.2 N_2O activation

The reduced 2Cu^I site formed after exchanging Cu^{2+} cations to ZSM-5 zeolite was reported to activate N_2O and O_2 to form the [Cu$_2$(μ-O)]$^{2+}$ active site.[101] In the case of N_2O

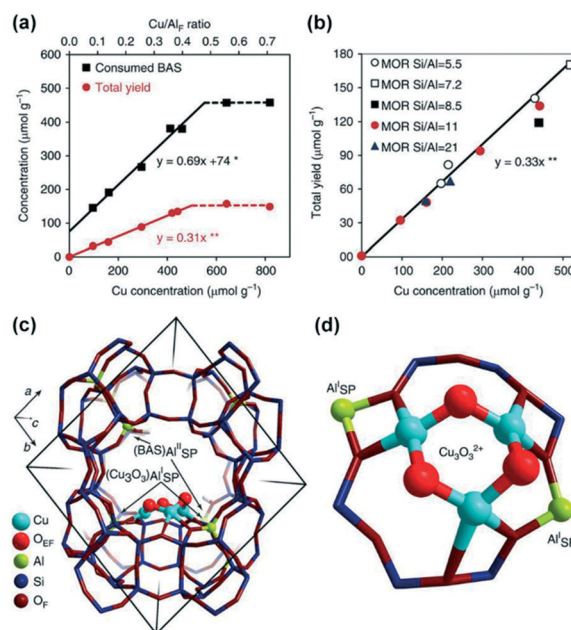**Fig. 10** (a) Concentration of Al cations as a function of the Cu/Al ratio for Cu-MOR with Si/Al = 11. (b) Total methanol yield as a function of Cu concentration. (c and d) [Cu$_3$(μ-O)$_3$]$^{2+}$ active site on the T2/T2 Al-pair site of the 8-MR side pocket of MOR. Adapted from ref. 47.

1754 | Catal. Sci. Technol., 2019, **9**, 1744–1768

This journal is © The Royal Society of Chemistry 2019

decomposition into an N_2 molecule released to the atmosphere and an oxo transferred to the 2Cu^I centers forming a $[Cu_2(\mu\text{-O})]^{2+}$, the N–O bond cleavage occurs in a straightforward fashion as it requires only two electrons that can be provided by the two Cu^I centers. Tsai *et al.*[125] carried out kinetics experiments to determine the activation energy for N_2O activation on Cu-ZSM-5 by measuring the reaction rate at six different temperatures ranging from 25 to 100 °C, following the previous work suggesting that the 22 700 cm^{-1} absorption feature ($[Cu_2(\mu\text{-O})]^{2+}$ formation) from N_2O activation is already observed at 100 °C.[101] The measured activation energy from the Arrhenius plot was reported to be $E_a = 2.5$ kcal mol^{-1}, which agrees very well with the DFT-calculated apparent activation barrier (2.0 kcal mol^{-1}, see Fig. 11).

Furthermore, Tsai *et al.* elaborated that there are three modes for the N_2O molecule to bind the two Cu^I centers separated by 4.17 Å.[125] These are the μ-1,1-O, μ-1,3-O,N and η^1-N binding modes. Although the latter binding mode results in the highest binding energy, it lacks a proper reaction coordinate to form a bridging oxo on the Cu centers. The μ-1,3-O,N binding mode, on the other hand, results in the second highest binding energy, but the required apparent activation energy for O–N_2 bond cleavage (5 kcal mol^{-1}) is higher than that *via* the μ-1,1-O binding mode (2 kcal mol^{-1}). The transition state for N–O cleavage preceded by the μ-1,1-O binding prefers the open-shell singlet state with an elongated N–O bond length from 1.21 Å to 1.46 Å and a bent N–N–O angle of 143° (Fig. 11).

4.3 O_2 activation

In contrast to the N_2O decomposition, O_2 activation requires four electrons to break the O=O bond. Unfortunately, the reduced 2Cu^I site in Cu-zeolites can provide only two electrons. Thus, two additional electrons from the spectator 2Cu^I site are required. The detailed mechanism for this reaction was reported by Smeets *et al.* (Fig. 12).[126] The authors observed UV-vis spectral changes when Cu-ZSM-5 is heated from 25 to

375 °C under O_2 atmosphere. Specifically, a 22 700 cm^{-1} absorption band is formed at 175 °C while the 29 000 cm^{-1} absorption band, which was observable below 175 °C, now disappears. The 22 700 cm^{-1} and 29 000 cm^{-1} bands correspond to the $[Cu_2(\mu\text{-O})]^{2+}$ active site and a precursor, respectively. The rR spectral analyses using oxygen isotopes of $^{16}O_2$ and $^{18}O_2$ show two vibrational frequencies, where one (isotope sensitive 736 cm^{-1}) indicates the O–O stretch and the other (isotope insensitive 269 cm^{-1}) indicates the Cu–Cu stretch (Fig. 12, green spectra). These vibrational features are the characteristic of a $\mu\text{-}\eta^2{:}\eta^2$-peroxo-Cu$_2^{II}$ species, which defines the precursor structure. Upon O_2 activation at high temperatures, these vibrational frequencies disappear, leading to the enhancement of 456 and 870 cm^{-1} vibrational frequencies (Fig. 12, blue spectra), which are respectively assigned to the symmetric and antisymmetric stretch of the $[Cu_2(\mu\text{-O})]^{2+}$ active species.[101] This suggests that upon O_2 activation, the $\mu\text{-}\eta^2{:}\eta^2$-peroxo-Cu$_2^{II}$ precursor transforms directly to a $[Cu_2(\mu\text{-O})]^{2+}$ active species, where two spectator Cu^I cations from a remote site should exist to provide additional two electrons required for breaking the peroxo bond.

The main issue associated with the mechanism described above is the fate of the second O atom of the precursor. Smeets *et al.* suggested that the second O atom, instead of forming a second $[Cu_2(\mu\text{-O})]^{2+}$ active species, interacts with the zeolite lattice that acts as a reservoir for mobile O atoms.[126] However, a recent DFT study by our group showed that when the second O atom interacts with the lattice O atom and forms a Si–O–O–Si fragment (Fig. 13a, **PC′** in route 1), the activation energy required for breaking the $\mu\text{-}\eta^2{:}\eta^2$-peroxo bond of the precursor is extremely high (59.7 kcal mol^{-1}).[127] At elevated temperature, the **PC′** structure may lead to a rapid O-atom exchange, where the lattice O atom (in black) forms a desorbed O_2 molecule with another lattice O atom or with the bridging O atom of the active site. On the other hand, the simultaneous formation of two neighboring $[Cu_2(\mu\text{-O})]^{2+}$ active sites (Fig. 13a, route 2) is energetically more favorable with an O–O bond activation barrier of only 10.5 kcal mol^{-1}. Comparing this value and the N_2O activation
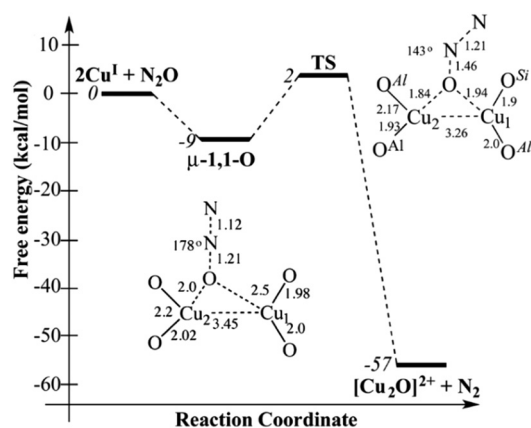
Fig. 11 DFT-calculated energy diagram for N_2O decomposition on 2[Cu]$^+$-ZSM-5 in the corresponding ground state. Reproduced with permission from ref. 125. Copyright 2014 American Chemical Society.
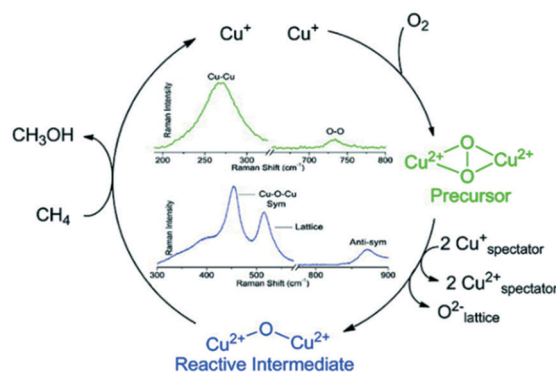
Fig. 12 Proposed reaction mechanism of O_2 activation on 2[Cu]$^+$-ZSM-5, forming a $[Cu_2(\mu\text{-O})]^{2+}$ active species (blue spectra) from a $\mu\text{-}\eta^2{:}\eta^2$-peroxo-Cu$_2^{II}$ precursor (green spectra). Adapted with permission from ref. 126. Copyright 2010 American Chemical Society.

This journal is © The Royal Society of Chemistry 2019

Catal. Sci. Technol., 2019, **9**, 1744–1768 | 1755

energy value (2.5 kcal mol^{-1})[125] to the minimum temperatures required for generating the $[Cu_2(\mu\text{-}O)]^{2+}$ active site from O_2 and N_2O activation (175 and 100 °C, respectively),[101] reasonable agreements can be suggested.

In the formation of the tricopper $[Cu_3(\mu\text{-}O)_3]^{2+}$ active site from O_2 activation of Cu-MOR, we recently suggested a $[Cu_2^I Cu^{II}O]^{2+}$ species as a theoretically possible precursor.[127] This species is formed as a consequence of two consecutive oxidations of methane over the tricopper active site.[111,127] In this case, since the precursor can provide four electrons required to break the O=O bond of the O_2 molecule, forming the $[Cu_2^{II} Cu^{III}(\mu\text{-}O)_3]^{2+}$ active species, no spectator Cu cations are needed. As shown in Fig. 13b, the reaction begins with the adsorption of an O_2 molecule on one Cu center of the precursor, followed by the formation of a $\mu\text{-}\eta^2{:}\eta^2$-peroxo-$Cu_3^{II}O$ intermediate species via a first transition state, requiring an activation energy of 24.2 kcal mol^{-1}. Subsequently, the peroxo bond of the intermediate species undergoes a cleavage with an activation barrier of only 10.4 kcal mol^{-1} to form the $[Cu_3(\mu\text{-}O)_3]^{2+}$ active site. Previously, the formation of an intermediate species was observed in experiments at high temperature, but its structure was unclear.[46] The $\mu\text{-}\eta^2{:}\eta^2$-peroxo-$Cu_3^{II}O$ species shown in Fig. 13b is a thermodynamically reasonable candidate structure for the intermediate species.

4.4 Reactivity of various Cu/O active site motifs

Similar to the reaction over Fe-exchanged zeolites, the methane hydroxylation by Cu-exchanged zeolites can also proceed via the homolytic and heterolytic HAA mechanisms.[18] Fig. 14

shows energy diagrams for the homolytic HAA mechanism of methane over a $[Cu_2(\mu\text{-}O)]^{2+}$ species hosted on the T3/T3 Al pair site within the zigzag 10-MR channel of the MFI zeolite framework. This site is energetically more stable than the T1/T1 Al pair site reported previously by our group.[112] The reaction begins with the adsorption of methane on the active site, preferring the triplet state. A homolytic C–H bond cleavage then takes place via a radical-like transition state (TS1) to form an intermediate structure involving a methyl radical. This process requires an activation energy of 14.8 kcal mol^{-1}, which agrees well with the experimental value (15.7 ± 0.5 kcal mol^{-1}).[101] The reactivity trend can actually be predicted by the stability of the O–H bond formed in the radical intermediate according to the Hammond–Leffler postulate,[131,132] where a stable, strong O–H bond usually leads to a low activation barrier and an early transition state, i.e. short C···H distance of TS1.[112] In the present case, the C···H distance of TS1 is 1.404 Å (Table S6†), which is 0.17 Å longer than that for methane activation by $[FeO]^{2+}$-ZSM-5 (see section 3.3), resulting in a higher C–H activation energy and a more endothermic formation of a methyl radical. The formed methyl radical is then recombined directly with the OH moiety, forming a methanol molecule bound to the Cu centers with a negligible activation barrier. The direct methanol desorption requires a very high energy of 52.6 kcal mol^{-1}, which is almost four times higher than the C–H activation barrier. This is mainly due to the high instability of two Cu^I centers formed on the reduced active site $[2Cu^I]^{2+}$-MFI.

An alternative HAA mechanism, where a lattice O atom near the active site acts as the active species abstracting the H atom of methane, was also recently reported by Sushkevich
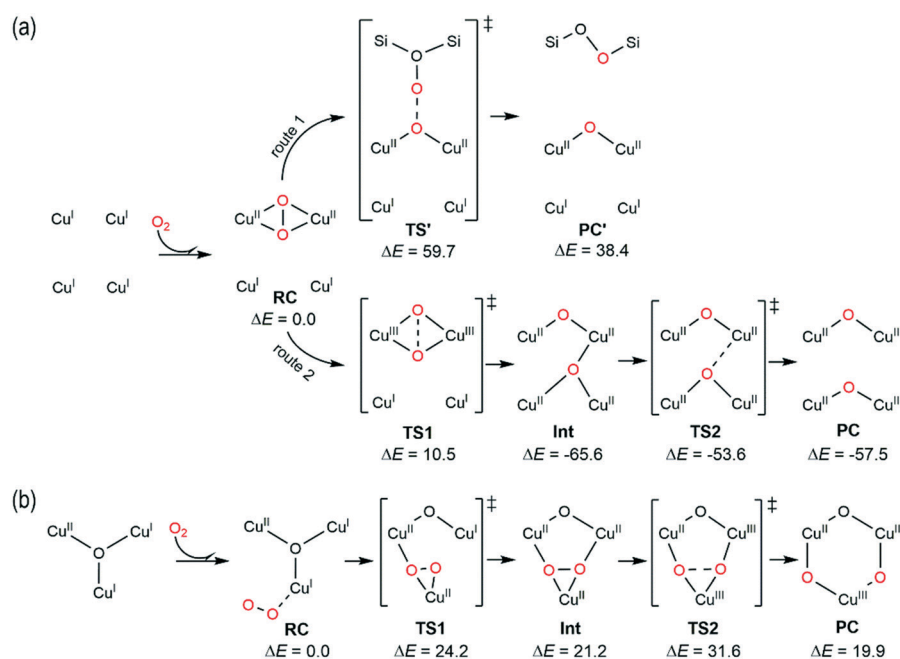
Fig. 13 DFT-predicted mechanisms of O_2 activation on (a) 4[Cu]$^+$-MOR and (b) $[Cu_3O]^{2+}$-MOR. Energies are given in kcal mol^{-1}. **RC**, **TS**, **Int**, and **PC** stand for reactant complex, transition state, reaction intermediate, and product complex, respectively. Adapted with permission from ref. 127. Copyright 2018 American Chemical Society.

1756 | Catal. Sci. Technol., 2019, 9, 1744–1768

This journal is © The Royal Society of Chemistry 2019

Fig. 14 DFT-calculated energy diagrams of methane hydroxylation by $[Cu_2(\mu\text{-O})]^{2+}$ hosted on the T3/T3 Al pair site of the zigzag 10-MR of ZSM-5 zeolite. Energies are given in kcal mol^{-1} and include the vdW-D2 dispersive correction.
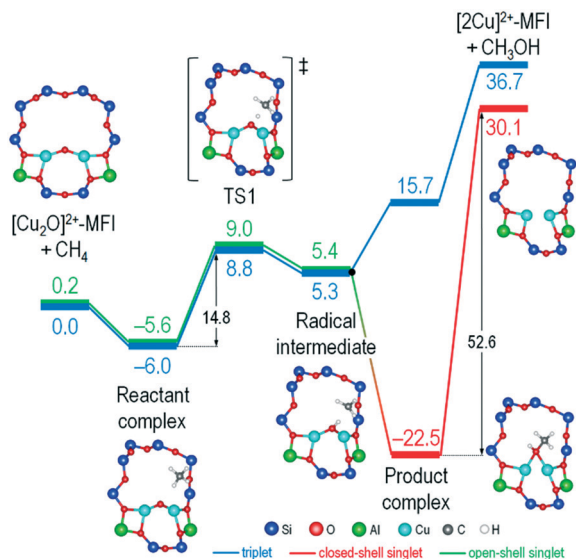
et al. for Cu-MOR.[19] Although this mechanism could explain the experimentally detected increase of the FTIR bands

assigned to Brønsted acid sites in the OH stretching region upon interaction with methane, the calculated C–H activation barrier (21.5 kcal mol^{-1})[19] is higher than that for the classical mechanism discussed above (18.9 kcal mol^{-1} in ref. 19, or 14.4 kcal mol^{-1} in ref. 111). This is expected since the lattice O atom has a spin density of nearly zero, which makes it less reactive. From a theoretical point of view, such a slight difference in activation barrier suggests that both mechanisms are possible to take place, although the classical mechanism is energetically more favorable for the low-temperature activation of methane.

Table 6 summarizes DFT-calculated methane C–H activation barriers and methanol desorption energies that have been reported so far for various motifs of Cu-oxo active sites in zeolites. Among them, the mononuclear $[CuO]^+$ and trinuclear $[Cu_3(\mu\text{-O})_3]^{2+}$ active sites are shown to require the lowest activation energies for cleaving the C–H bond of methane. The dinuclear $[Cu_2(\mu\text{-O})]^{2+}$ active site, on the other hand, shows a broad range of C–H activation barrier from 9.4 to 22.2 kcal mol^{-1}. We also notice that the bis(μ-O)dicopper $[Cu_2^{III}(\mu\text{-O})_2]^{2+}$ (O···O = 2.152 Å), which was originally proposed as the active site in Cu-ZSM-5 and Cu-MOR,[41] surprisingly shows a low C–H activation barrier (12.0 kcal mol^{-1}). The spin inversion from the closed-shell singlet state to the triplet state, known as two-state

Table 6 DFT-calculated methane activation barriers and methanol desorption energies reported so far for methane hydroxylation by various Cu/O active site motifs in zeolites

Active site motif	Zeolite framework	Al site(s)	Computational method[a]	C–H cleavage mechanism	C–H activation barrier (kcal mol^{-1})	MeOH desorption energy (kcal mol^{-1})	Ref.
$[CuO]^+$	MFI	10-MR(T1)	P/PBE-D2	Heterolytic	7.2	42.2	91
	CHA	8-MR	P/BEEF-vdW	Homolytic	11.7	—	115
$[CuOH]^+$	CHA	8-MR	P/BEEF-vdW	Homolytic	26.3	—	115
$[CuOO]^+$	CHA	8-MR	P/BEEF-vdW	Homolytic	37.1	—	115
$[Cu_2(\mu\text{-O})]^{2+}$	MFI	10-MR	C/B3LYP	Homolytic	18.5	—	101
	MFI	8-MR(T7/T12)	P/PBE	Homolytic	22.2	37.3	128
	MFI	10-MR	C/PBE	Homolytic	10.4	34.6	99
	MFI	10-MR(T1/T1)	P/PBE-D2	Homolytic	17.0	50.8[b]	112
	MFI	10-MR(T3/T3)	P/PBE-D2	Homolytic	14.8	52.6	This work
	MOR	8-MR(T2/T2)	P/BEEF-vdW	Homolytic	15.1	—	129
		8-MR(T4/T4)			21.5		
	MOR	8-MR(T2/T2)	P/PBE-D2	Homolytic	10.9	54.0 (28.8)[d]	111
		8-MR(T4/T4)			14.4	60.4 (26.5)[d]	
	MOR	8-MR	P/PBE0-TS	Homolytic	21.5[c]	(9.6)[d]	19
				Homolytic	18.9[c]	32.5	
	MAZ	8-MR(T1/T1)	P/PBE-D2	Homolytic	11.8	53.2 (30.1)[d]	111
	CHA	8-MR(T1/T1)	P/PBE-D2	Homolytic	11.4	56.6[b]	112
	AEI	8-MR(T1/T1)	P/PBE-D2	Homolytic	9.4	40.6[b]	112
	AFX	8-MR(T1/T1)	P/PBE-D2	Homolytic	11.6	52.1[b]	112
$[Cu_2(\mu\text{-O})_2]^{2+}$	MFI	10-MR(T3/T3)	P/PBE-D2	Homolytic	12.0[e]	19.8	This work
$[Cu_3(\mu\text{-O})_3]^{2+}$	MFI	8-MR(T7/T12)	P/PBE	Homolytic	12.9	20.6	128
	MOR	8-MR(T2/T2)	P/PBE	Homolytic	17.7	—	47
	MOR	8-MR(T2/T2)	P/PBE-D2	Homolytic	7.6, 13.7[f]	21.3, 24.5[f]	111
	MOR	8-MR(T2/T2)	P/PBE	Homolytic	8.8, 17.7, 18.6[f]	—	130
	MOR	8-MR	P/PBE0-TS	Homolytic	14.8[c]	(13.9)[d]	19
	MAZ	8-MR(T1/T1)	P/PBE-D2	Homolytic	6.2, 11.7[f]	23.5, 22.1[f]	111

[a] Structure/functional-dispersion correction; C and P stand for cluster model and periodic structure, respectively. [b] Recalculated data including the vdW-D2 dispersion correction. [c] Apparent activation barrier measured from the initial structure (Cu/O)Z + CH$_4$, no formation of reactant complex. [d] Values in parentheses are water-assisted methanol desorption energies. [e] The calculated energy diagrams and optimized structures are available in the ESI. [f] Various active O atoms.

This journal is © The Royal Society of Chemistry 2019

Catal. Sci. Technol., 2019, **9**, 1744–1768 | **1757**

reactivity,[133,134] is found to play an important role in stabilizing the transition state and radical intermediate structures (see Fig. S2†), consistent with the previous DFT work for pMMO.[106] Besides a facile C–H activation, the bis(μ-O)Cu$_2^{III}$ also desorbs methanol with a low desorption energy (19.8 kcal mol^{-1}), which is even lower than the water-assisted methanol desorption energy on the reduced [2Cu]$^{2+}$ site (see section 4.5). Considering the fact that the formed methanol can also be extracted at room temperature,[43] it is thermodynamically possible that the bis(μ-O)Cu$_2^{III}$ is also present as the active site in Cu-ZSM-5 despite the general lack of clear spectroscopy evidence on the presence of Cu^{III} ions from either XAS or Raman.[135,136]

It is also shown in Table 6 that the [Cu$_2$(μ-O)]$^{2+}$ hosted on the T2/T2 and T4/T4 Al pair sites of MOR activates methane with different C–H activation energies. We have previously suggested that such distinct reactivities are related to the geometry (i.e. Cu–O–Cu angle) of the active site, which

affects the molecular orbitals responsible for the H-atom abstraction of methane.[112] To gain deeper insight into the effects of ∠CuOCu on the reactivity, let us discuss the molecular orbitals (MOs) of [Cu$_2$(μ-O)]$^{2+}$ hosted on the T2/T2 and T4/T4 Al pair sites of MOR,[111] hereinafter referred to as [Cu$_2$O]$^{2+}$-MOR(1) (∠CuOCu = 89.2°) and -MOR(2) (∠CuOCu = 140.7°), respectively. Fig. 15 shows two singly occupied molecular orbitals (SOMOs) of [Cu$_2$O]$^{2+}$-MOR(1) and -MOR(2) in the triplet state as well as their energies for the α and β spins (orange and blue lines, respectively). Each SOMO is composed of an occupied α-$\pi^*_{x/y/z}$ orbital and an unoccupied β-$\pi^*_{x/y/z}$ antibonding orbital. In Fig. 15 (RC), it is shown that the β-spin SOMO in [Cu$_2$O]$^{2+}$-MOR(1) is higher in energy than those in [Cu$_2$O]$^{2+}$-MOR(2), indicating stronger antibonding interactions that result in slightly longer Cu–O–Cu bonds (1.772 Å versus 1.748 Å).[111] However, the opposite is observed for the α-spin SOMOs, as we predicted previously.[18]
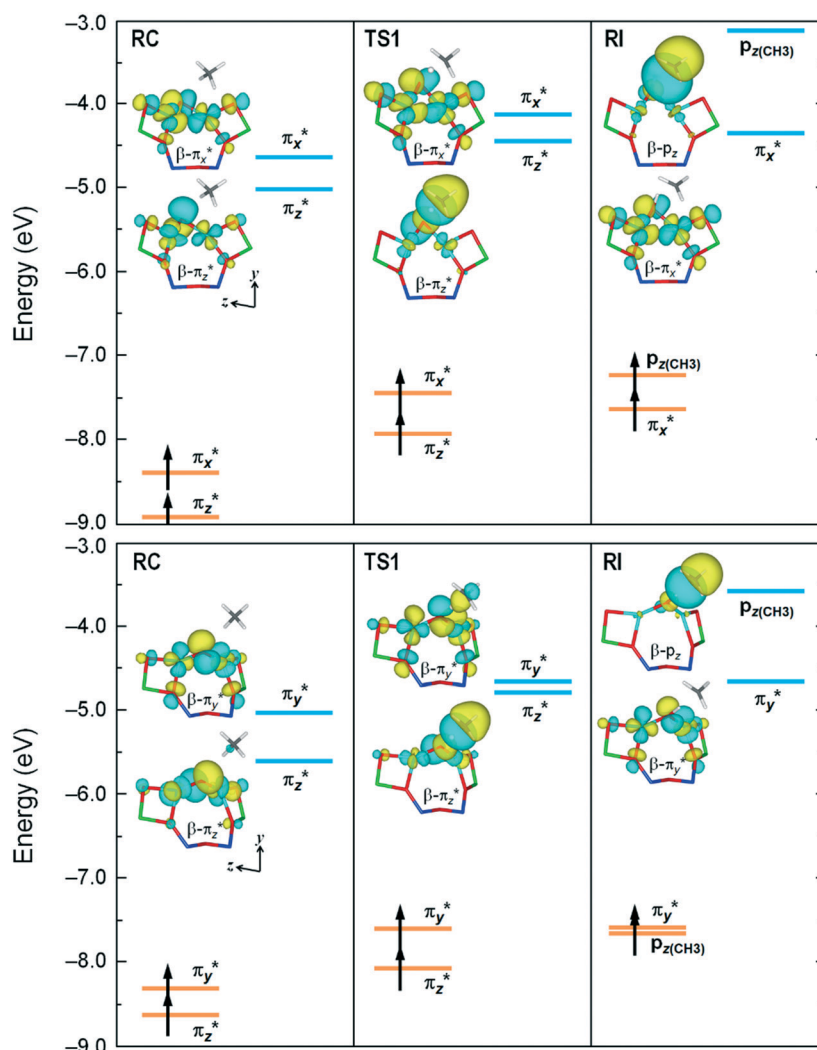

Fig. 15 Frontier molecular orbitals (MOs) of [Cu$_2$O]$^{2+}$-MOR(1) with ∠CuOCu = 89.2° (top) and [CuO]$^{2+}$-MOR(2) with ∠CuOCu = 140.7° (bottom) in the triplet state, and MO energies for the α and β spins (orange and blue lines, respectively). RC, TS1, and RI stand for reactant complex, first transition state, and radical intermediate, respectively. π^*_x, π^*_y and π^*_z correspond to (Cu d$_{xy}$–O p$_x$), (Cu d$_{xy}$–O p$_y$), and (Cu d$_{xz}$–O p$_z$) antibonding orbitals, respectively. Frontier MOs in the α spin are similar to those in the β spin and thus not shown for simplicity.

In the transition state of C–H bond cleavage, we expect one of the two empty SOMOs, *i.e.* $\beta\text{-}\pi_x^*/\beta\text{-}\pi_y^*$ and $\beta\text{-}\pi_z^*$ orbitals, to interact with the highest occupied molecular orbital (HOMO) of methane, since these orbitals are much lower in energy than the lowest unoccupied molecular orbital of the α spin (α-LUMO). Indeed, we found in Fig. 15 (**TS1**) that the $\beta\text{-}\pi_z^*$ orbital interacts most significantly with the p_z orbital of H···CH$_3$. Specifically, the H···CH$_3$ p_z orbital is repulsed back by the antibonding interaction formed with the O p_z orbital. Such a repulsive interaction between the donor and the acceptor orbitals is found to be stronger in $[Cu_2O]^{2+}$-MOR(1) than in $[Cu_2O]^{2+}$-MOR(2), as indicated by the higher energies of the $\beta\text{-}\pi_z^*$ orbital (−4.46 eV *versus* −4.80 eV). This is the reason for the longer O···H distance (1.209 Å) but shorter H···C distance (1.357 Å) in the **TS1** of $[Cu_2O]^{2+}$-MOR(1), as compared to those in the **TS1** of $[Cu_2O]^{2+}$-MOR(2) (1.184 and 1.395 Å, respectively).[111] This makes **TS1** of $[Cu_2O]^{2+}$-MOR(1) an earlier and lower-lying transition state than that of $[Cu_2O]^{2+}$-MOR(2). Consequently, the calculated C–H activation barrier of methane for $[Cu_2O]^{2+}$-MOR(1) (10.9 kcal mol^{-1}) is lower than that for $[Cu_2O]^{2+}$-MOR(2) (14.4 kcal mol^{-1}).[111]

In Fig. 15 (**RI**), where a methyl radical and a OH moiety are formed, we found that one of the SOMOs is now originated from the p_z orbital of CH$_3^{\cdot}$ (methyl radical has a doublet ground state with a C-atom spin density of about 0.9).[111] Moreover, we also found a newly formed σ_{OH} bonding orbital (O p_z + H s) at lower energies (not shown in Fig. 15). This orbital determines the stability of the formed OH bond. The σ_{OH} energies of $[Cu_2O]^{2+}$-MOR(1) (−14.67 and −14.63 eV, respectively for the α and β spins) are found to be lower than those for $[Cu_2O]^{2+}$-MOR(2) (−14.27 and −14.11 eV, respectively), which clearly suggest that the small $\angle$CuOCu in $[Cu_2O]^{2+}$-MOR(1) leads to a more stable formation of **RI** (ΔE = 8.1 *versus* 10.5 kcal mol^{-1} relative to **RC**)[111] and thus to a more facile HAA of methane.

Corma and co-workers suggested that a destabilization of the donor orbital of a molecule, due to zeolite confinement, can ease the charge transfers and thus lower the activation barrier.[137,138] We previously demonstrated that confining a methane molecule in various pure silica zeolites indeed increases the HOMO energy of methane by about 0.9 eV,[112] which becomes one of the reasons for the low C–H activation barrier of methane. In the case of $[Cu_2O]^{2+}$-MOR(1) and -MOR(2), however, the difference in C–H activation barrier more dominantly originates from the $\angle$CuOCu rather than the confinement effect, since the methane is confined in the same zeolite framework and at the same 12-MR site.

Besides the active site geometry and zeolite confinement, another factor influencing the reactivity is the spin density of the active O atom. We previously showed that in the quartet high-spin state of $[Cu_3(\mu\text{-}O)_3]^{2+}$-MOR, the two in-plane μ-O atoms have similar spin densities (0.40–0.49), which are lower than that for the out-of-plane μ-O atom (0.90, see Fig. 16).[111] While the O atoms with a lower spin density require a methane's C–H activation barrier of about 13.7 kcal mol^{-1}, the O atom with a higher spin density leads to a lower

activation barrier of 7.6 kcal mol^{-1}.[111,130] More comprehensive discussions of alkane activation by metal-oxo complexes with different O-atom spin densities can be found elsewhere.[139] The active O-atom spin density, however, cannot be directly correlated with the reactivity of different metal active sites, as recently demonstrated by Liu *et al.*[140] through DFT investigations on bimetallic $[Cu_2M(\mu\text{-}O)_3]^{2+}$-MFI (M = Fe, Co, Ni, Cu). Instead, the authors suggested an energetic parameter of hydrogen affinity (E_H) as a better descriptor for the reactivity of various metal active sites since the homolytic C–H bond cleavage of methane correlates well with the thermodynamic stability of the CH$_3^{\cdot}$···HO radical intermediate. This descriptor assumes that the interaction between the CH$_3^{\cdot}$ and the catalyst is so weak that the ability of the active site to accept the H atom dominates the stability of the radical intermediate.[141] Despite this, Liu *et al.* also reminded that deviations might be observed when using this descriptor because E_H omits the effects of the radical OH interaction between the generated methyl radical and the reduced active site.[140] Another bimetallic $[Cu–O–M]^{2+}$-MFI (M = Cu, Ag, Zn, Au) was also recently investigated using DFT calculations.[142] Among these, the $[Cu–O–Ag]^{2+}$-MFI was found to have the highest spin density at the active O atom and the highest stability of the radical intermediate, which result in the lowest C–H activation energy of methane.

4.5 Water-assisted methanol desorption

Table 6 shows that methanol desorption from the $[2Cu]^{2+}$ site, a reduced form of the $[Cu_2(\mu\text{-}O)]^{2+}$, requires desorption energies that are approximately four times higher than the C–H activation barrier of methane, which makes methanol difficult to desorb and prone to over-oxidation. Such high energies are mainly due to the strong Cu–O bonds and the instability of the 2Cu^I centers. Therefore, as discussed in section 2.3, the choice of solvent and method for methanol extraction becomes very important. In the most recent studies using the stepwise approach, it can be seen from Table 2 that the online extraction method with steam (often carried out at the same temperature as in the previous CH$_4$ loading

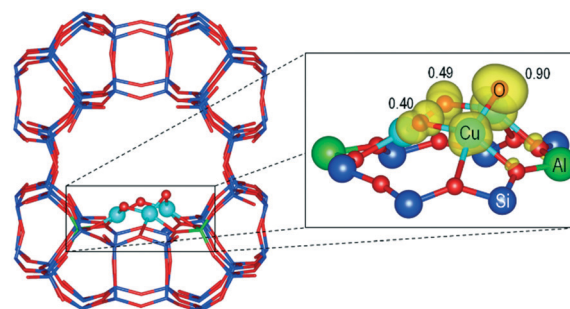**Fig. 16** $[Cu_3(\mu\text{-}O)_3]^{2+}$ active site on the 8-MR side pocket of MOR zeolite, showing its μO-atom spin densities (yellow lobes) on the right. Reproduced with permission from ref. 18. Copyright 2018 American Chemical Society.

This journal is © The Royal Society of Chemistry 2019

Catal. Sci. Technol., 2019, **9**, 1744–1768 | **1759**

step) is better for high methanol productivity and selectivity than the off-line extraction method with water. We have theoretically shown that when a water molecule is added to the $[Cu_2(CH_3OH)]^{2+}$-MOR product complex, it is bound strongly to the $2Cu^I$ centers, replacing the position of the formed methanol molecule and thus reducing the high desorption energy of methanol by half (from 60.4 to 26.5 kcal mol^{-1}).[111] However, this reduced value is still too high for methanol to desorb at room temperature. This explains why steam (about 200 °C), as compared to water, is more preferred for methanol extraction.

Sushkevich et al.[19] recently reported that water acts not only as a solvent for methanol extraction but also as an oxygen source for the regeneration of the $[Cu_2(\mu\text{-}O)]^{2+}$ active site and for the formation of H_2 ($2Cu^I + H_2O \rightarrow Cu_2^{II}O + H_2$), although its plausibility is still debated.[144,145] The debates seem to be reasonable since the formation of H_2 from such a reaction, theoretically, requires a very high activation barrier (69.0 kcal mol^{-1})[111] and is less favorable than the direct H_2O desorption from the $2Cu^I$ centers which requires less energy (53.4 kcal mol^{-1}).[111] Nonetheless, it has been recently shown that the anaerobic methane hydroxylation on Cu-MOR yields more methanol with a higher methanol selectivity than the aerobic one,[118] indicating a high favorability of H_2O as the oxidant.

5. Methane hydroxylation by Co/zeolites

5.1 Active site structures

The DR-UV-vis spectra of O_2-activated Co-ZSM-5 prepared by ion-exchange and impregnation methods were reported to determine the Co speciation.[53] As shown in Fig. 17 (lines a and b), two catalyst samples prepared by the ion-exchange method show absorption bands at 15 000, 17 000, and 21 500 cm^{-1},[53] which are known to be the signature peaks of the Co^{II} cation located at three different sites of ZSM-5.[146] The first absorption feature is in good agreement with the 15 900 cm^{-1} absorption band assigned to the α-Fe^{II} sitting on the β-type 6-MR site of *BEA zeolite.[75] The Co-ZSM-5 prepared by the impregnation method (Fig. 17, line c), however, shows a broad band between 18 000 and 26 000 cm^{-1} as well as a narrow band at 13 500 cm^{-1}, indicating the formation of Co$_3$O$_4$ clusters.[53] Moreover, there are also two absorption bands at 8000 and 19 600 cm^{-1}, corresponding to the presence of CoO species, which are not observed in lines a and b of Fig. 17. This sample, after calcination at 550 °C in a flow of N$_2$ and O$_2$, activates methane at 150 °C to yield 0.4 μmol g-cat^{-1} of methanol with 100% selectivity (off-line extraction method in ethanol).[53]

To this end, the active site structure of the activated Co-ZSM-5 is unclear since no DR-UV-vis spectra of the CH$_4$-reacted Co-ZSM-5 have been reported for distinguishing the bands corresponding to the Co active site from those corresponding to the spectator inactive Co site. However, Nakamura et al. recently suggested from XANES spectra and
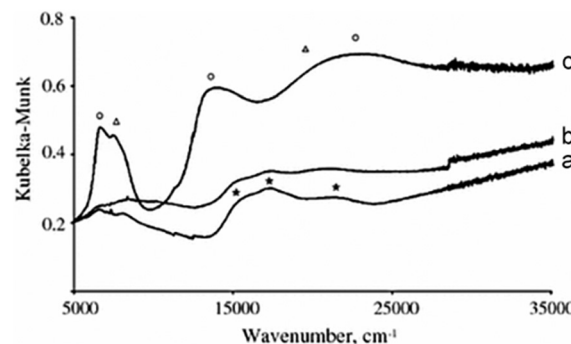

Fig. 17 DR-UV-vis spectra of Co-ZSM-5 prepared (a and b) by ion-exchange method with different mass fractions of Co (0.9 and 2.7 wt%, respectively) and (c) by an impregnation method after calcination at 550 °C in a flow of N$_2$ and O$_2$. Adapted from ref. 53.

EXAFS analysis that the Co speciation in the inactivated (reduced) Co-ZSM-5 is a mononuclear Co^{II} species.[147] From this suggestion, we can hypothesize several O_2-oxidized structures of the active site. Considering that O_2 requires four electrons to break its O=O bond, a $[Co^{IV}O]^{2+}$ species would be an unreasonable candidate for the active site, unless two additional electrons can be provided from the spectator Co^{II} site, as previously suggested for the formation of $Cu_2^{II}O$-ZSM-5 from $2Cu^I$-ZSM-5 and O_2.[126,127] Alternatively, a $[Co^{II}OH]^+$ species derived from dehydration of the catalyst during O_2 activation, as previously suggested for $[CuOH]^+$-SSZ-13 (see section 4.1),[117] is also a theoretically possible active site.

5.2 Reactivity of various Co/O active site motifs

In Table 7, we summarize DFT-calculated methane activation barriers and methanol desorption energies for methane hydroxylation by various Co/O active site motifs in ZSM-5 zeolite. Among the presented active sites, the Co cations in $[Co^{III}O]^+$, $[Co^{II}OH]^+$, and $[Co_2^{II}(\mu\text{-}O)]^{2+}$ active sites are reduced to highly unstable Co^I centers after oxidizing methane to methanol. Thus, these active site motifs are rather unrealistic for Co-ZSM-5. On the contrary, the $[Co^{IV}O]^{2+}$ and $[Co_2^{III}(\mu\text{-}O)_2]^{2+}$ seem to be more plausible active sites since they are reduced to stable Co^{II} centers after the methanol formation. Comparing the reactivity of these two active sites (see also Fig. S4†), we found that the $[CoO]^{2+}$ active site requires a much less activation energy for cleaving the C–H bond of methane, i.e. only 6.5 kcal mol^{-1}, which is comparable to that for $[FeO]^{2+}$-ZSM-5 (7.0 kcal mol^{-1}) discussed in section 3.3.

Fig. 18 shows the detailed energy diagrams of methane hydroxylation over $[CoO]^{2+}$-ZSM-5 (Co–O = 1.598 Å) in the doublet low-spin and quartet high-spin states. In the quartet ground state, the Co and O atoms have spin densities of 2.00 and 0.69 (Table S7†), respectively, suggesting that the active site has an electronic structure of $[Co^{III}\text{-}O^{\bullet-}]^{2+}$, instead of $[Co^{IV}O]^{2+}$. The reactant complex is formed preferably in the quartet state with an adsorption energy of −5.3 kcal mol^{-1}. The subsequent homolytic C–H bond cleavage via TS1 also prefers the quartet state with a low activation barrier of 6.5

1760 | Catal. Sci. Technol., 2019, 9, 1744–1768

This journal is © The Royal Society of Chemistry 2019

Table 7 DFT-calculated methane activation barriers and methanol desorption energies reported so far for methane hydroxylation by various Co/O active site motifs in zeolites

Active site motif	Zeolite framework	Al site(s)	Computational method[a]	C–H cleavage mechanism	C–H activation barrier (kcal mol^{-1})	MeOH desorption energy (kcal mol^{-1})	Ref.
[CoO]$^+$	MFI	10-MR(T1)	P/PBE-D2	Heterolytic	17.1	41.7	91
	MFI	—	C/B3LYP	Homolytic	15.0[b]	19.0	143
[CoO]$^{2+}$	MFI	δ-6MR(T11/T11)	P/PBE-D2	Homolytic	6.5	30.3	This work
[CoOH]$^+$	MFI	10-MR(T1)	P/PBE-D2	Heterolytic	21.2[c]	—	This work
[Co$_2$(μ-O)]$^{2+}$	MFI	10-MR	C/PBE	Heterolytic	19.1	36.9	99
[Co$_2$(μ-O)$_2$]$^{2+}$	MFI	10-MR(T3/T3)	P/PBE-D2	Homolytic	27.2[c]	10.8	This work

[a] Structure/functional-dispersion correction; C and P stand for cluster model and periodic structure, respectively. [b] Apparent activation barrier measured from the initial structure (Co/O)Z + CH$_4$, no formation of reactant complex. [c] The calculated energy diagrams and optimized structures are available in the ESI.

kcal mol^{-1} and a short C···H bond distance of 1.213 Å. With such an early transition state, it is expected that the formation of the O–H bond and methyl radical in the intermediate structure would be slightly endothermic (ΔE of 2.4 kcal mol^{-1} relative to the reactant complex). The formation of the product complex of methanol via a low-barrier **TS2** is very stable in the quartet ground state with a quite strong Co–OHCH$_3$ bond (1.986 Å), which unfortunately leads to a high methanol desorption energy of 30.3 kcal mol^{-1}. Nonetheless, the overall reaction is highly exothermic by −22.5 kcal mol^{-1}.

6. Methane hydroxylation by Ni/zeolites

6.1 Active site structures

Shan et al.[54] reported UV-vis spectra of Ni-ZSM-5 showing the appearance of a 22 800 cm^{-1} absorption band after O$_2$ activation at 600 °C (Fig. 19a). The absence of this band from the

Fig. 18 DFT-calculated energy diagrams of methane hydroxylation by [CoO]$^{2+}$ hosted on the T11/T11 Al pair site of the δ-type 6-MR of ZSM-5 zeolite. Energies are given in kcal mol^{-1} and include the vdW-D2 dispersive correction.

inactivated Ni-ZSM-5 and H-ZSM-5 indicates that Ni-oxo active sites are formed during the O$_2$ activation at high temperature (>280 °C). Moreover, the gradual disappearance of the band after CH$_4$ activation during a given time (Fig. 19b) indicates a dissociation of the oxo atom(s) from the Ni center(s) to form oxygenate products, e.g. methanol. The 22 800 cm^{-1} absorption feature found in Ni-ZSM-5 is different from the 25 000 cm^{-1} absorption band assigned to the bis(μ-oxo)dinickel [Ni$_2$(μ-O)$_2$]$^{2+}$ complex in amine ligands,[148] but similar to the 22 700 cm^{-1} absorption band assigned to the mono(μ-oxo)dicopper in ZSM-5 zeolite after being initially thought to be the bis(μ-oxo)dicopper.[41,101] Moreover, with the EXAFS analyses for the O$_2$-activated catalyst at 400 °C showing a Ni-center coordination number of 2.5 ± 0.5, the active site is thus concluded to have a mono(μ-oxo)dinickel [Ni$_2$(μ-O)]$^{2+}$ structure (Fig. 19c).[54] However, it is surprising that the Ni coordination number remains the same after the reaction with methane to yield methanol.

It was reported that the highest yield and best selectivity for the production of methanol from CH$_4$ oxidation by Ni-ZSM-5 are achieved at a reaction temperature of 175 °C.[54] Despite this, the kinetics analysis was conducted at temperatures ranging from 280 to 330 °C, showing an Arrhenius plot where a C–H activation energy of methane is measured to be 19.9 kcal mol^{-1},[54] which is slightly higher than that for [Cu$_2$(μ-O)]$^{2+}$-ZSM-5 (15.7 ± 0.5 kcal mol^{-1}).[101] However, DFT calculations showed that the [Ni$_2$(μ-O)]$^{2+}$ active site in a periodic structure of ZSM-5 zeolite requires high activation energies to abstract the H atom of methane (35.2 or 38.9 kcal mol^{-1}).[16,149] This makes the reaction difficult to proceed at low temperature. Given such computational predictions and the possibility that the 22 800 cm^{-1} absorption band might also correspond to the bis(μ-oxo)dinickel as well as the ambiguous Ni–O coordination numbers reported in ref. 54, the actual active site structure in the O$_2$-activated Ni-ZSM-5 can be considered unclear.

6.2 Reactivity of various Ni/O active site motifs

The reported methane C–H activation barriers and methanol desorption energies for various Ni/O active site motifs in zeolites are summarized in Table 8. This table shows that only
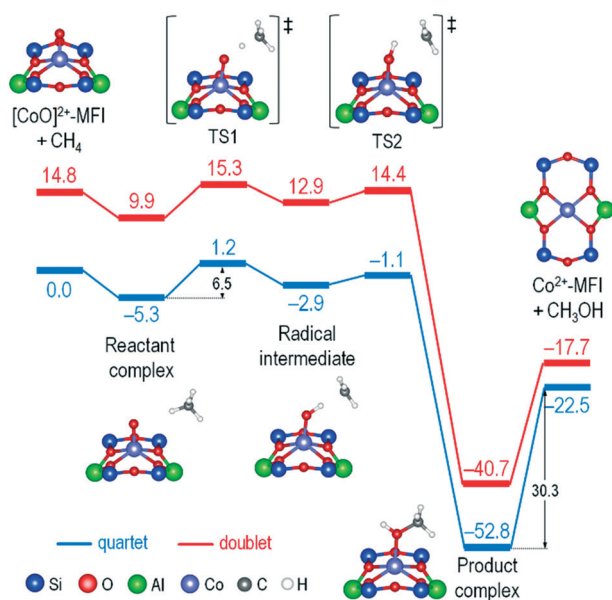
This journal is © The Royal Society of Chemistry 2019

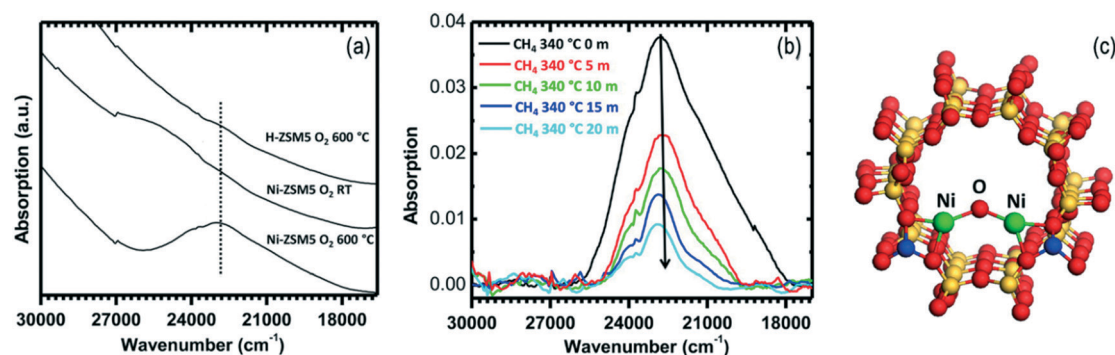Catal. Sci. Technol., 2019, **9**, 1744–1768 | **1761**

Fig. 19 (a) UV-vis spectra of Ni-ZSM-5 and H-ZSM-5 after O_2 activation at room temperature and 600 °C. (b) Decrease in the intensity of the 22 800 cm^{-1} band after reaction with CH_4 at 340 °C for various durations of time. (c) $[Ni_2(\mu\text{-}O)]^{2+}$ on the 10-MR of the MFI zeolite framework. Adapted with permission from ref. 54. Copyright 2014 American Chemical Society.

$[NiO]^+$, $[Ni_2(\mu\text{-}O)_2]^{2+}$, and $[Ni_3(\mu\text{-}O)_3]^{2+}$ species can cleave the C–H bond of methane with activation energies ranging from 15 to 20 kcal mol^{-1} (experimental value:[54] 19.9 kcal mol^{-1}). The $[Ni_2(\mu\text{-}O)_2]^{2+}$- and $[Ni_3(\mu\text{-}O)_3]^{2+}$-MFI, in particular, are also capable of desorbing methanol from the Ni centers with low desorption energies of 11.4 and 19.8 kcal mol^{-1}, respectively, rendering them suitable for a spontaneous yield of methanol without any extraction procedures needed.

Fig. 20 shows the recently reported energy diagrams of methane hydroxylation by $[Ni_2(\mu\text{-}O)_2]^{2+}$-ZSM-5 (the O1 atom acts as the active species) calculated using the DFT+U method.[149] As shown in this figure, the $[Ni_2(\mu\text{-}O)_2]^{2+}$ active site has a ground state of open-shell singlet state, where the unpaired electron from one Ni^{III} center is antiferromagnetically coupled with that from another Ni^{III} center. A methane molecule is adsorbed on the active site with an adsorption energy of −4.9 kcal mol^{-1} and is then activated *via* a radical-like transition state (**TS1**) where one of the H atoms is abstracted to form an OH moiety and a methyl radical with an activation energy (15.3 kcal mol^{-1}) similar to that calculated for $[Cu_2(\mu\text{-}O)]^{2+}$-ZSM-5 (see also Fig. 15). Here, the separation C⋯H distance of **TS1** was reported to be 1.283 Å. Subsequently, a barrierless HO–CH$_3$ recombination takes place to

form a product complex with rather long Ni–O bonds (about 2.3 Å), due to an electronic effect where the Ni centers prefer to strongly bind the negatively charged O^{2-} anion (O2 in Fig. 21) rather than the fully coordinated O atom of neutral methanol. Along with the high stability of two Ni^{II} centers formed in the reduced active site, such loose Ni–O bonds cause the desorption energy of methanol to be low, even lower than the C–H activation barrier of methane.

In Fig. 21, we show energy diagrams for the formation of a $[Ni_2(\mu\text{-}O)_2]^{2+}$ active site from O_2 activation on the reduced $[2Ni]^{2+}$-ZSM-5. Following the mechanism presented in Fig. 13a (route 2), the diagrams suggest that the O_2 molecule is strongly bound to the Ni centers in a $\mu\text{-}\eta^2\text{:}\eta^2$-peroxo-Ni$_2^{II}$ fashion with a binding energy of −83.0 kcal mol^{-1} and an elongated O–O bond length of 1.517 Å, which is 0.31 Å longer than that in the gas phase. Subsequently, the peroxo bond is cleaved *via* a **TS** with an activation barrier of 22.5 kcal mol^{-1} and a separation O⋯O distance of 1.724 Å, the former of which indicates that the reaction is energetically possible to proceed. During the cleavage, the ground state is changed from the quintet state to the open-shell singlet state, where both of the Ni centers have the same magnitude but different directions of spin (see Table S8†). The bis(μ-oxo)Ni$_2^{III}$ is then

Table 8 DFT-calculated methane activation barriers and methanol desorption energies reported so far for methane hydroxylation by various Ni/O active site motifs in zeolites

Active site motif	Zeolite framework	Al site(s)	Computational method[a]	C–H cleavage mechanism	C–H activation barrier (kcal mol^{-1})	MeOH desorption energy (kcal mol^{-1})	Ref.
$[NiO]^+$	MFI	10-MR(T1)	P/PBE-D2	Heterolytic	15.7	38.7	91
	MOR	—	P/BEEF-vdW	Homolytic	19.1[b]	—	16
$[NiO]^{2+}$	MFI	δ-6MR(T11/T11)	P/PBE-D2	Homolytic	4.5	26.6	149
$[NiOH]^+$	MOR	—	P/BEEF-vdW	Homolytic	38.2[b]	—	16
$[Ni_2(\mu\text{-}O)]^{2+}$	MFI	10-MR	C/PBE	Heterolytic	14.1	32.3	99
	MFI	10-MR(T3/T3)	P/PBE-D2	Homolytic	38.9	53.5	149
	MOR	—	P/BEEF-vdW	Homolytic	35.2[b]	—	16
$[Ni_2(\mu\text{-}O)_2]^{2+}$	MFI	10-MR(T3/T3)	P/PBE-D2	Homolytic	15.3, 20.2[c]	11.4, 13.1[c]	149
	MOR	—	P/BEEF-vdW	Homolytic	17.8[b]	—	16
$[Ni_3(\mu\text{-}O)_3]^{2+}$	MFI	8-MR(T7/T12)	P/PBE-D2	Homolytic	18.2, 20.0[c]	19.8, 14.5[c]	149
	MOR	—	P/BEEF-vdW	Homolytic	25.6[b]	—	16

[a] Structure/functional-dispersion correction; C and P stand for cluster model and periodic structure, respectively. [b] Approximated from the reported diagrams. [c] Various active O atoms.
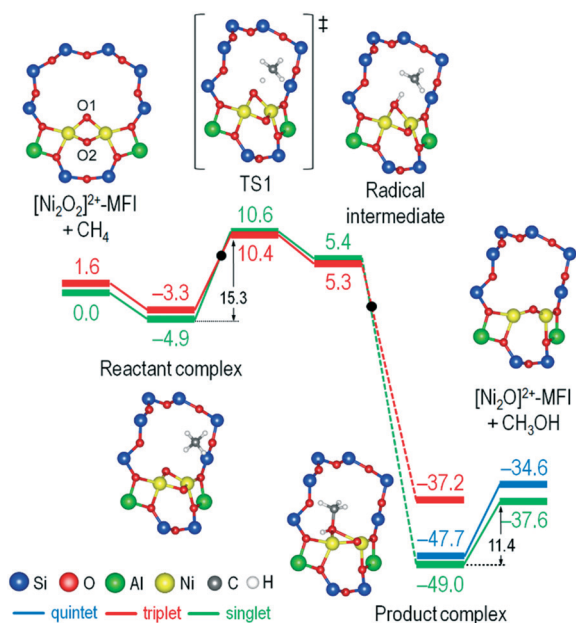
1762 | *Catal. Sci. Technol.*, 2019, **9**, 1744–1768

This journal is © The Royal Society of Chemistry 2019

Fig. 20 Energy diagrams calculated by the DFT+U method for methane hydroxylation by $[Ni_2(\mu\text{-}O)_2]^{2+}$ active species hosted on the T3/T3 Al pair site of the zigzag 10-MR in ZSM-5 zeolite. Adapted by permission of ref. 149. The Royal Society of Chemistry.
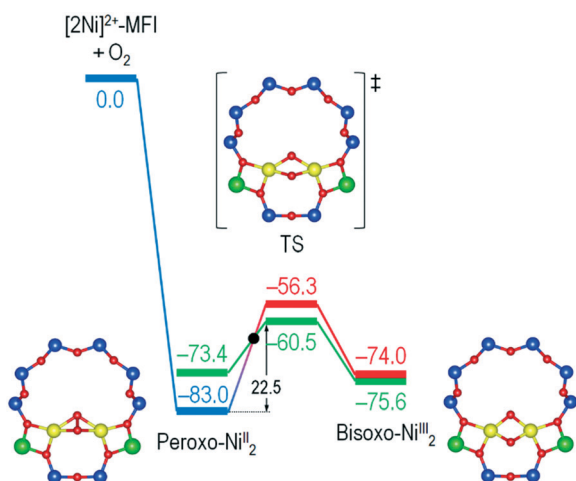

Fig. 21 Energy diagrams calculated by the DFT+U method (U = 4.0 eV) for O_2 activation over $[2Ni]^{2+}$-MFI (T3/T3 Al pair site). Legends for the atomic and line colors are as in Fig. 20.

formed with a further separation O···O distance of 2.207 Å. The overall reaction is highly exothermic by −75.6 kcal mol⁻¹.

7. Concluding remarks

In this review, we have summarized the recent spectroscopy and computational findings in the active site structures of Fe-, Cu-, Co- and Ni-exchanged zeolites. We have also discussed the formation as well as the reactivity and its influencing factors of the proposed active sites. While the Fe- and Cu-zeolites have been thoroughly characterized in experiments with the stron-

gest candidates for the active site being the $[FeO]^{2+}$ and $[Cu_2(\mu\text{-}O)]^{2+}$ or $[Cu_3(\mu\text{-}O)_3]^{2+}$, respectively, the other two metal–zeolite catalysts are still inadequately studied and thus should be explored more in-depth to open new possibilities of more reactive and effective catalysts. The $[Ni_2(\mu\text{-}O)_2]^{2+}$-ZSM-5, for example, has been predicted by DFT calculations to activate methane and desorb methanol with low activation and desorption energies, which are two combined features that cannot be found in $[FeO]^{2+}$-, $[Cu_2(\mu\text{-}O)]^{2+}$- and $[Cu_3(\mu\text{-}O)_3]^{2+}$-ZSM-5. The probable challenge in this direction, however, is the preparation of the metal–zeolite catalyst with a homogeneous distribution of a particular active site structure.

DFT calculations have guided us to the rational design of metal-exchanged zeolite catalysts for methane hydroxylation, although questions related to the ground state of the active sites still remain unsolved due to the practical use of computational catalysis which requires finding a compromise between realistic models and accurate methods[150] that can satisfy both the computational cost and the results. Nonetheless, here by observing the energy trends, we have understood some key points that affect the reactivity of $[FeO]^{2+}$-, $[Cu_2(\mu\text{-}O)]^{2+}$- and $[Cu_3(\mu\text{-}O)_3]^{2+}$-zeolites toward methane. They are (i) active site geometry, (ii) zeolite confinement on methane, (iii) spin density of the active O-atom and (iv) hydrogen affinity of the active site. Item (i), in particular, may enable one to "play" with different sizes and structures of the zeolite ring hosting the active site for delivering the best performance of the active site. Thus, it will be intriguing to see how various zeolite frameworks alter the geometry and reactivity of the active site.

While the best performance of metal-exchanged zeolites in oxidizing methane to methanol is today achieved with the stepwise approach, a number of unsolved questions related to the process remain: (a) the mechanism of active site formation from abundant oxidants (e.g. O_2 and H_2O) and the distribution of active sites in zeolites are not well understood, (b) the search for catalysts and/or methods that allow a facile and solvent-free methanol extraction is lacking, and (c) practical strategies for combating the trade-off between methane conversion rate and methanol selectivity have not been found. To address issues (a) and (b), thermodynamic and kinetic analyses from DFT calculations might be useful for aiding in the interpretations of experimental observations and further identifying several key points that can be improved. To obtain reliable DFT results, however, one needs to use realistic models (i.e. periodic structure) of zeolites instead of small cluster models because the zeolite micropores exhibit unneglectable confinement effects on the reaction. The use of relatively accurate yet computationally inexpensive methods (e.g. meta-GGA functionals) is also encouraged. For issue (c), in addition to the methanol protection and methanol collector approaches suggested previously,[21,151] optimization of the reaction conditions and duration at each reaction step is also indispensable.

It is also worth noting that metal–organic frameworks (MOFs) have been recently reported to be active for methane

This journal is © The Royal Society of Chemistry 2019

Catal. Sci. Technol., 2019, **9**, 1744–1768 | **1763**

selective oxidation to methanol at low temperature.[152–154] Notably, mono(μ-OH)diiron in MIL-53, [Cu$_3$(OH)$_4$]$^{2+}$ in NU-1000 and bis(μ-O)dicopper in MOF-808 were reported to be stable after oxidative activation using H$_2$O$_2$ at 60 °C, O$_2$ at 200 °C and N$_2$O at 150 °C, respectively.[152–154] Unlike zeolites, MOFs typically exhibit higher metal loadings,[14] which allow designing novel active phases with higher density of active sites for methane activation. Moreover, MOFs possess an organic component that is suitable for installing various functional groups by using postsynthetic methods (*i.e.* chemical modifications performed on the fabricated material rather than on the molecule precursors).[155] The functionalization of MOFs for the direct methane conversion to methanol will undoubtedly open new opportunities for achieving a low-temperature activation of the catalysts and a high conversion rate of methane.

8. Computational methods

The energy diagrams shown in Fig. 4, 5, 14, 18 and 21 and the ESI† were calculated using periodic structures and the calculations were performed with fixed spin-multiplicities under the Kohn–Sham formulation[156,157] as implemented in the Vienna *Ab initio* Simulation Package (VASP).[158,159] The projector augmented wave (PAW) method was employed to describe the interaction between ion cores and electrons.[160,161] The electron exchange correlation was treated by the generalized gradient approximation (GGA) based on the Perdew–Burke–Ernzerhof (PBE) functional.[162] The meta-GGA functional of MS1,[163,164] which improves the description of noncovalent interactions over PBE, was also used to calculate FeO-ZSM-5 presented in Table 3 (entry 3). The plane wave basis sets with a cut-off energy of 550 eV were used for all calculations. Brillouin zone sampling was restricted to the Γ point only. The semiempirical Grimme's D2 method was employed to account for van der Waals (vdW) dispersive correction.[165] The conjugate gradient method was employed to optimize intermediate structures, while the climbing-image nudged elastic band (CI-NEB) method was used to locate transition states.[166] The image-dependent pair potentials (IDPP) method was employed to generate the NEB images.[167] Both geometry optimizations and CI-NEB calculations were considered to be converged when the maximum forces on all atoms were less than 0.05 eV Å^{-1}. During calculations, all atoms were allowed to fully relax. Atomic spin densities were calculated by using the Bader analysis algorithm[168] and optimized structures were visualized by using VESTA.[169]

The spin densities of FeO-ZSM-5 presented in Table 3 (entry 4) and the MOs of Cu$_2$O-ZSM-5 shown in Fig. 15 were calculated using hydrogen-terminated cluster models constructed from the corresponding optimized periodic structures[111] (Fig. S5 and S6†). Spin-unrestricted DFT calculations were performed by using the HSE06 (ref. 170 and 171) or B3LYP[172–174] hybrid functional. The 6-311+G* basis set[175,176] was used for the Fe and Cu atoms, while the D95** basis set was used for the Si, Al, O, C and H atoms. During the geometry optimizations of FeO-ZSM-5, the eight Si atoms were fixed while the other atoms were allowed to fully relax. During the MO calculations of Cu$_2$O-ZSM-5, in contrast, only the terminating H atoms were allowed to fully relax, while the remaining atoms were fixed to their optimized positions. Grimme's vdW-D2 correction was also taken into account.[165] The MOs were visualized by using VESTA,[169] while the MO energies were obtained by using ChemCraft.[177]

Abbreviations

AlPO	Aluminum phosphate
B3LYP	Becke 3-parameter, Lee–Yang–Parr functional
BEEF	Bayesian error estimation functional
DR-UV-vis	Diffuse reflectance ultraviolet visible
EPR	Electron paramagnetic resonance
EXAFS	Extended X-ray absorption fine structure
FTIR	Fourier-transform infrared
GGA	Generalized gradient approximation
HAA	H-atom abstraction
HSE	Hyde–Scuseria–Ernzerhof functional
MCD	Magnetic circular dichroism
MS1	Made simple one functional
PBE	Perdew–Burke–Ernzerhof functional
rR	Resonance Raman
SAPO	Silicon-aluminophosphate
SSZ	Standard-oil synthetic zeolite
TS (vdW)	Tkatchenko–Scheffler dispersion correction
vdW	van der Waals
XANES	X-ray absorption near edge structure
XAS	X-ray absorption spectroscopy
XES	X-ray emission spectroscopy
ZSM	Zeolite Socony Mobil

Conflicts of interest

There are no conflicts to declare.

Acknowledgements

References

1 R. A. Kerr, *Science*, 2010, **328**, 1624–1626.
2 T. A. Moore, *Int. J. Coal Geol.*, 2012, **101**, 36–81.

3 Y. Konno, T. Fujii, A. Sato, K. Akamine, M. Naiki, Y. Masuda, K. Yamamoto and J. Nagao, *Energy Fuels*, 2017, **31**, 2607–2616.

4 Y. Shen, Y. Zhan, S. Li, F. Ning, Y. Du, Y. Huang, T. He and X. Zhou, *Chem. Sci.*, 2017, **8**, 7498–7504.

5 Z. Zakaria and S. K. Kamarudin, *Renewable Sustainable Energy Rev.*, 2016, **65**, 250–261.

6 U. Olsbye, S. Svelle, M. Bjørgen, P. Beato, T. V. W. Janssens, F. Joensen, S. Bordiga and K. P. Lillerud, *Angew. Chem., Int. Ed.*, 2012, **51**, 5810–5831.

7 H. D. Gesser, N. R. Hunter and C. B. Prakash, *Chem. Rev.*, 1985, **85**, 235–244.

8 A. I. Olivos-Suarez, À. Szécsényi, E. J. M. Hensen, J. Ruiz-Martinez, E. A. Pidko and J. Gascon, *ACS Catal.*, 2016, **6**, 2965–2981.

9 N. Dietl, M. Engeser and H. Schwarz, *Chem. – Eur. J.*, 2010, **16**, 4452–4456.

10 A. C. Rosenzweig, C. A. Frederick, S. J. Lippard and P. Nordlund, *Nature*, 1993, **366**, 537–543.

11 R. L. Lieberman and A. C. Rosenzweig, *Nature*, 2005, **434**, 177–182.

12 S. I. Chan, K. H.-C. Chen, S. S.-F. Yu, C.-L. Chen and S. S.-J. Kuo, *Biochemistry*, 2004, **43**, 4421–4430.

13 P. Tomkins, M. Ranocchiari and J. A. van Bokhoven, *Acc. Chem. Res.*, 2017, **50**, 418–425.

14 K. T. Dinh, M. M. Sullivan, P. Serna, R. J. Meyer, M. Dincă and Y. Román-Leshkov, *ACS Catal.*, 2018, **8**, 8306–8313.

15 B. E. R. Snyder, M. L. Bols, R. A. Schoonheydt, B. F. Sels and E. I. Solomon, *Chem. Rev.*, 2018, **118**, 2718–2768.

16 A. R. Kulkarni, Z.-J. Zhao, S. Siahrostami, J. K. Nørskov and F. Studt, *Catal. Sci. Technol.*, 2018, **8**, 114–123.

17 E. Borfecchia, P. Beato, S. Svelle, U. Olsbye, C. Lamberti and S. Bordiga, *Chem. Soc. Rev.*, 2018, **47**, 8097–8133.

18 M. H. Mahyuddin, Y. Shiota, A. Staykov and K. Yoshizawa, *Acc. Chem. Res.*, 2018, **51**, 2382–2390.

19 V. L. Sushkevich, D. Palagin, M. Ranocchiari and J. A. van Bokhoven, *Science*, 2017, **356**, 523–527.

20 C. Hammond, S. Conrad and I. Hermans, *ChemSusChem*, 2012, **5**, 1668–1686.

21 M. Ravi, M. Ranocchiari and J. A. van Bokhoven, *Angew. Chem., Int. Ed.*, 2017, **56**, 16464–16483.

22 C. Hammond, M. M. Forde, M. H. Ab Rahim, A. Thetford, Q. He, R. L. Jenkins, N. Dimitratos, J. A. Lopez-Sanchez, N. F. Dummer, D. M. Murphy, A. F. Carley, S. H. Taylor, D. J. Willock, E. E. Stangland, J. Kang, H. Hagen, C. J. Kiely and G. J. Hutchings, *Angew. Chem., Int. Ed.*, 2012, **51**, 5129–5133.

23 C. Hammond, N. Dimitratos, J. A. Lopez-Sanchez, R. L. Jenkins, G. Whiting, S. A. Kondrat, M. H. ab Rahim, M. M. Forde, A. Thetford, H. Hagen, E. E. Stangland, J. M. Moulijn, S. H. Taylor, D. J. Willock and G. J. Hutchings, *ACS Catal.*, 2013, **3**, 1835–1844.

24 C. Hammond, I. Hermans and N. Dimitratos, *ChemCatChem*, 2015, **7**, 434–440.

25 C. Baerlocher and L. B. McCusker, *Database of Zeolite Structures*, http://www.iza-structure.org/databases/, (accessed 26 July 2018).

26 C. Baerlocher, L. B. McCusker and D. H. Olson, *Atlas of zeolite framework types*, Elsevier, Amsterdam, 6th edn., 2007.

27 M. Iwamoto, H. Furukawa, Y. Mine, F. Uemura, S. Mikuriya and S. Kagawa, *J. Chem. Soc., Chem. Commun.*, 1986, 1272–1273.

28 J. Li, H. Chang, L. Ma, J. Hao and R. T. Yang, *Catal. Today*, 2011, **175**, 147–156.

29 A. M. Beale, F. Gao, I. Lezcano-Gonzalez, C. H. F. Peden and J. Szanyi, *Chem. Soc. Rev.*, 2015, **44**, 7371–7405.

30 M. H. M. Ahmed, O. Muraza, A. K. Jamil, E. N. Shafei, Z. H. Yamani and K.-H. Choi, *Energy Fuels*, 2017, **31**, 5482–5490.

31 A. Galadima and O. Muraza, *J. Ind. Eng. Chem.*, 2018, **61**, 265–280.

32 B. M. Weckhuysen and J. Yu, *Chem. Soc. Rev.*, 2015, **44**, 7022–7024.

33 W. Loewenstein, *Am. Mineral.*, 1954, **39**, 92–96.

34 B. Xing, J. Ma, R. Li and H. Jiao, *Catal. Sci. Technol.*, 2017, **7**, 5694–5708.

35 A. Corma, *Chem. Rev.*, 1995, **95**, 559–614.

36 C. Liu, I. Tranca, R. A. van Santen, E. J. M. Hensen and E. A. Pidko, *J. Phys. Chem. C*, 2017, **121**, 23520–23530.

37 V. I. Sobolev, K. A. Dubkov, O. V. Panna and G. I. Panov, *Catal. Today*, 1995, **24**, 251–252.

38 E. V. Starokon, M. V. Parfenov, S. S. Arzumanov, L. V. Pirutko, A. G. Stepanov and G. I. Panov, *J. Catal.*, 2013, **300**, 47–54.

39 E. V. Starokon, M. V. Parfenov, L. V. Pirutko, S. I. Abornev and G. I. Panov, *J. Phys. Chem. C*, 2011, **115**, 2155–2161.

40 M. L. Bols, S. D. Hallaert, B. E. R. Snyder, J. Devos, D. Plessers, H. M. Rhoda, M. Dusselier, R. A. Schoonheydt, K. Pierloot, E. I. Solomon and B. F. Sels, *J. Am. Chem. Soc.*, 2018, **140**, 12021–12032.

41 M. H. Groothaert, P. J. Smeets, B. F. Sels, P. A. Jacobs and R. A. Schoonheydt, *J. Am. Chem. Soc.*, 2005, **127**, 1394–1395.

42 M. J. Wulfers, R. F. Lobo, B. Ipek and S. Teketel, *Chem. Commun.*, 2015, **51**, 4447–4450.

43 M. B. Park, S. H. Ahn, M. Ranocchiari and J. van Bokhoven, *ChemCatChem*, 2017, **9**, 3705–3713.

44 T. Sheppard, C. D. Hamill, A. Goguet, D. W. Rooney and J. M. Thompson, *Chem. Commun.*, 2014, **50**, 11053–11055.

45 K. Narsimhan, K. Iyoki, K. Dinh and Y. Román-Leshkov, *ACS Cent. Sci.*, 2016, **2**, 424–429.

46 Y. Kim, T. Y. Kim, H. Lee and J. Yi, *Chem. Commun.*, 2017, **53**, 4116–4119.

47 S. Grundner, M. A. C. Markovits, G. Li, M. Tromp, E. A. Pidko, E. J. M. Hensen, A. Jentys, M. Sanchez-Sanchez and J. A. Lercher, *Nat. Commun.*, 2015, **6**, 7546.

48 D. K. Pappas, A. Martini, M. Dyballa, K. Kvande, S. Teketel, K. A. Lomachenko, R. Baran, P. Glatzel, B. Arstad, G. Berlier, C. Lamberti, S. Bordiga, U. Olsbye, S. Svelle, P. Beato and E. Borfecchia, *J. Am. Chem. Soc.*, 2018, **140**, 15270–15278.

49 V. L. Sushkevich and J. A. van Bokhoven, *Catal. Sci. Technol.*, 2018, **8**, 4141–4150.

50 P. Tomkins, A. Mansouri, S. E. Bozbag, F. Krumeich, M. B. Park, E. M. C. Alayon, M. Ranocchiari and J. A. van Bokhoven, *Angew. Chem.*, 2016, **128**, 5557–5561.

This journal is © The Royal Society of Chemistry 2019

Catal. Sci. Technol., 2019, **9**, 1744–1768 | **1765**

51   D. K. Pappas, E. Borfecchia, M. Dyballa, I. Pankin, K. A. Lomachenko, A. Martini, M. Signorile, S. Teketel, B. Arstad, G. Berlier, C. Lamberti, S. Bordiga, U. Olsbye, K. P. Lillerud, S. Svelle and P. Beato, *J. Am. Chem. Soc.*, 2017, **139**, 14961–14975.

52   B. Ipek and R. F. Lobo, *Chem. Commun.*, 2016, **52**, 13401–13404.

53   N. V. Beznis, B. M. Weckhuysen and J. H. Bitter, *Catal. Lett.*, 2010, **136**, 52–56.

54   J. Shan, W. Huang, L. Nguyen, Y. Yu, S. Zhang, Y. Li, A. I. Frenkel and F. Tao, *Langmuir*, 2014, **30**, 8558–8569.

55   G. I. Panov, V. I. Sobolev and A. S. Kharitonov, *J. Mol. Catal.*, 1990, **61**, 85–97.

56   G. I. Panov, V. I. Sobolev, K. A. Dubkov, V. N. Parmon, N. S. Ovanesyan, A. E. Shilov and A. A. Shteinman, *React. Kinet. Catal. Lett.*, 1997, **61**, 251–258.

57   P. J. Smeets, M. H. Groothaert and R. A. Schoonheydt, *Catal. Today*, 2005, **110**, 303–309.

58   P. Tomkins, A. Mansouri, V. L. Sushkevich, L. I. van der Wal, S. E. Bozbag, F. Krumeich, M. Ranocchiari and J. A. van Bokhoven, *Chem. Sci.*, 2019, **10**, 167–171.

59   N. V. Beznis, A. N. C. van Laak, B. M. Weckhuysen and J. H. Bitter, *Microporous Mesoporous Mater.*, 2011, **138**, 176–183.

60   Y. K. Krisnandi, B. A. P. Putra, M. Bahtiar, Z. Zahara, I. Abdullah and R. F. Howe, *Procedia Chem.*, 2015, **14**, 508–515.

61   J. Shan, M. Li, L. F. Allard, S. Lee and M. Flytzani-Stephanopoulos, *Nature*, 2017, **551**, 605–608.

62   A. Oda, T. Ohkubo, T. Yumura, H. Kobayashi and Y. Kuroda, *Inorg. Chem.*, 2019, **58**, 327–338.

63   A. Oda, T. Ohkubo, T. Yumura, H. Kobayashi and Y. Kuroda, *Angew. Chem., Int. Ed.*, 2017, **56**, 9715–9718.

64   G. I. Panov, G. A. Sheveleva, A. S. Kharitonov, V. N. Romannikov and L. A. Vostrikova, *Appl. Catal., A*, 1992, **82**, 31–36.

65   K. Yoshizawa, Y. Shiota, T. Yumura and T. Yamabe, *J. Phys. Chem. B*, 2000, **104**, 734–740.

66   P. Marturano, L. Drozdová, A. Kogelbauer and R. Prins, *J. Catal.*, 2000, **192**, 236–247.

67   A. A. Battiston, J. H. Bitter and D. C. Koningsberger, *Catal. Lett.*, 2000, **66**, 75–79.

68   A. A. Battiston, J. H. Bitter and D. C. Koningsberger, *J. Catal.*, 2003, **218**, 163–177.

69   J. Jia, Q. Sun, B. Wen, L. X. Chen and W. M. H. Sachtler, *Catal. Lett.*, 2002, **82**, 7–11.

70   H. Xia, K. Sun, K. Sun, Z. Feng, W. X. Li and C. Li, *J. Phys. Chem. C*, 2008, **112**, 9001–9005.

71   B. R. Wood, J. A. Reimer, A. T. Bell, M. T. Janicke and K. C. Ott, *J. Catal.*, 2004, **224**, 148–155.

72   B. R. Wood, J. A. Reimer, A. T. Bell, M. T. Janicke and K. C. Ott, *J. Catal.*, 2004, **225**, 300–306.

73   K. Jíša, J. Nováková, M. Schwarze, A. Vondrová, S. Sklenák and Z. Sobalik, *J. Catal.*, 2009, **262**, 27–34.

74   S. Sklenak, P. C. Andrikopoulos, B. Boekfa, B. Jansang, J. Nováková, L. Benco, T. Bucko, J. Hafner, J. Dědeček and Z. Sobalík, *J. Catal.*, 2010, **272**, 262–274.

75   B. E. R. Snyder, P. Vanelderen, M. L. Bols, S. D. Hallaert, L. H. Böttger, L. Ungur, K. Pierloot, R. A. Schoonheydt, B. F. Sels and E. I. Solomon, *Nature*, 2016, **536**, 317–321.

76   B. E. R. Snyder, L. H. Böttger, M. L. Bols, J. J. Yan, H. M. Rhoda, A. B. Jacobs, M. Y. Hu, J. Zhao, E. E. Alp, B. Hedman, K. O. Hodgson, R. A. Schoonheydt, B. F. Sels and E. I. Solomon, *Proc. Natl. Acad. Sci. U. S. A.*, 2018, 201721717.

77   K. A. Dubkov, N. S. Ovanesyan, A. A. Shteinman, E. V. Starokon and G. I. Panov, *J. Catal.*, 2002, **207**, 341–352.

78   G. I. Panov, K. A. Dubkov and E. V. Starokon, *Catal. Today*, 2006, **117**, 148–155.

79   S. D. Hallaert, M. L. Bols, P. Vanelderen, R. A. Schoonheydt, B. F. Sels and K. Pierloot, *Inorg. Chem.*, 2017, **56**, 10681–10690.

80   V. I. Sobolev, G. I. Panov, A. S. Kharitonov, V. N. Romannikov, A. M. Volodin and K. G. Ione, *J. Catal.*, 1993, **139**, 435–443.

81   E. V. Starokon, K. A. Dubkov, L. V. Pirutko and G. I. Panov, *Top. Catal.*, 2003, **23**, 137–143.

82   M. H. Mahyuddin, Y. Shiota, A. Staykov and K. Yoshizawa, *Inorg. Chem.*, 2017, **56**, 10370–10380.

83   G. Li, E. A. Pidko, I. A. W. Filot, R. A. van Santen, C. Li and E. J. M. Hensen, *J. Catal.*, 2013, **308**, 386–397.

84   E. V. Kondratenko and J. Pérez-Ramírez, *J. Phys. Chem. B*, 2006, **110**, 22586–22595.

85   G. D. Pirngruber, J.-D. Grunwaldt, J. A. van Bokhoven, A. Kalytta, A. Reller, O. V. Safonova and P. Glatzel, *J. Phys. Chem. B*, 2006, **110**, 18104–18107.

86   G. D. Pirngruber, J.-D. Grunwaldt, P. K. Roy, J. A. van Bokhoven, O. Safonova and P. Glatzel, *Catal. Today*, 2007, **126**, 127–134.

87   A. Rosa, G. Ricciardi and E. J. Baerends, *Inorg. Chem.*, 2010, **49**, 3866–3880.

88   F. Buda, B. Ensing, M. C. M. Gribnau and E. J. Baerends, *Chem. – Eur. J.*, 2003, **9**, 3436–3444.

89   L. Wang, T. Maxisch and G. Ceder, *Phys. Rev. B: Condens. Matter Mater. Phys.*, 2006, **73**, 195107.

90   F. Göltl, C. Michel, P. C. Andrikopoulos, A. M. Love, J. Hafner, I. Hermans and P. Sautet, *ACS Catal.*, 2016, **6**, 8404–8409.

91   M. H. Mahyuddin, A. Staykov, Y. Shiota and K. Yoshizawa, *ACS Catal.*, 2016, **6**, 8321–8331.

92   K. Yoshizawa, *Acc. Chem. Res.*, 2006, **39**, 375–382.

93   Á. Szécsényi, G. Li, J. Gascon and E. A. Pidko, *ACS Catal.*, 2018, **8**, 7961–7972.

94   K. Yoshizawa, Y. Shiota and T. Yamabe, *Organometallics*, 1998, **17**, 2825–2831.

95   T. Yumura and K. Yoshizawa, *Organometallics*, 2001, **20**, 1397–1407.

96   S. Li, Y. Wang, T. Wu and W. F. Schneider, *ACS Catal.*, 2018, **8**, 10119–10130.

97   E. Kurnaz, M. F. Fellah and I. Onal, *Microporous Mesoporous Mater.*, 2011, **138**, 68–74.

98   M. He, J. Zhang, X.-L. Sun, B.-H. Chen and Y.-G. Wang, *J. Phys. Chem. C*, 2016, **120**, 27422–27429.

99   A. A. Arvidsson, V. P. Zhdanov, P.-A. Carlsson, H. Grönbeck and A. Hellman, *Catal. Sci. Technol.*, 2017, **7**, 1470–1477.

100   J. K. Kirkland, S. N. Khan, B. Casale, E. Miliordos and K. D. Vogiatzis, *Phys. Chem. Chem. Phys.*, 2018, **20**, 28786–28795.

101 J. S. Woertink, P. J. Smeets, M. H. Groothaert, M. A. Vance, B. F. Sels, R. A. Schoonheydt and E. I. Solomon, *Proc. Natl. Acad. Sci. U. S. A.*, 2009, **106**, 18908–18913.

102 R. S. Czernuszewicz, J. E. Sheats and T. G. Spiro, *Inorg. Chem.*, 1987, **26**, 2063–2067.

103 R. Balasubramanian, S. M. Smith, S. Rawat, L. A. Yatsunyk, T. L. Stemmler and A. C. Rosenzweig, *Nature*, 2010, **465**, 115–119.

104 Y. Shiota and K. Yoshizawa, *Inorg. Chem.*, 2009, **48**, 838–845.

105 Y. Shiota, G. Juhász and K. Yoshizawa, *Inorg. Chem.*, 2013, **52**, 7907–7917.

106 J. C. S. Da Silva, R. C. R. Pennifold, J. N. Harvey and W. R. Rocha, *Dalton Trans.*, 2016, **45**, 2492–2504.

107 P. Vanelderen, B. E. R. Snyder, M.-L. Tsai, R. G. Hadt, J. Vancauwenbergh, O. Coussens, R. A. Schoonheydt, B. F. Sels and E. I. Solomon, *J. Am. Chem. Soc.*, 2015, **137**, 6383–6392.

108 M. A. Newton, A. J. Knorpp, A. B. Pinar, V. L. Sushkevich, D. Palagin and J. A. van Bokhoven, *J. Am. Chem. Soc.*, 2018, **140**, 10090–10093.

109 A. J. Knorpp, M. A. Newton, A. B. Pinar and J. A. van Bokhoven, *Ind. Eng. Chem. Res.*, 2018, **57**, 12036–12039.

110 B. E. R. Snyder, P. Vanelderen, R. A. Schoonheydt, B. F. Sels and E. I. Solomon, *J. Am. Chem. Soc.*, 2018, **140**, 9236–9243.

111 M. H. Mahyuddin, T. Tanaka, Y. Shiota, A. Staykov and K. Yoshizawa, *ACS Catal.*, 2018, **8**, 1500–1509.

112 M. H. Mahyuddin, A. Staykov, Y. Shiota, M. Miyanishi and K. Yoshizawa, *ACS Catal.*, 2017, **7**, 3741–3751.

113 B. Ipek, M. J. Wulfers, H. Kim, F. Göltl, I. Hermans, J. P. Smith, K. S. Booksh, C. M. Brown and R. F. Lobo, *ACS Catal.*, 2017, **7**, 4291–4303.

114 R. Oord, J. E. Schmidt and B. M. Weckhuysen, *Catal. Sci. Technol.*, 2018, **8**, 1028–1038.

115 A. R. Kulkarni, Z.-J. Zhao, S. Siahrostami, J. K. Nørskov and F. Studt, *ACS Catal.*, 2016, **6**, 6531–6536.

116 F. Giordanino, E. Borfecchia, K. A. Lomachenko, A. Lazzarini, G. Agostini, E. Gallo, A. V. Soldatov, P. Beato, S. Bordiga and C. Lamberti, *J. Phys. Chem. Lett.*, 2014, **5**, 1552–1559.

117 E. Borfecchia, K. A. Lomachenko, F. Giordanino, H. Falsig, P. Beato, A. V. Soldatov, S. Bordiga and C. Lamberti, *Chem. Sci.*, 2015, **6**, 548–563.

118 V. L. Sushkevich, D. Palagin and J. A. van Bokhoven, *Angew. Chem., Int. Ed.*, 2018, **57**, 8906–8910.

119 F. Giordanino, P. N. R. Vennestrøm, L. F. Lundegaard, F. N. Stappen, S. Mossin, P. Beato, S. Bordiga and C. Lamberti, *Dalton Trans.*, 2013, **42**, 12741.

120 S. Grundner, W. Luo, M. Sanchez-Sanchez and J. A. Lercher, *Chem. Commun.*, 2016, **52**, 2553–2556.

121 A. A. Verma, S. A. Bates, T. Anggara, C. Paolucci, A. A. Parekh, K. Kamasamudram, A. Yezerets, J. T. Miller, W. N. Delgass, W. F. Schneider and F. H. Ribeiro, *J. Catal.*, 2014, **312**, 179–190.

122 D. Palagin, A. J. Knorpp, A. B. Pinar, M. Ranocchiari and J. A. van Bokhoven, *Nanoscale*, 2017, **9**, 1144–1153.

123 C. Paolucci, A. A. Parekh, I. Khurana, J. R. Di Iorio, H. Li, J. D. Albarracin Caballero, A. J. Shih, T. Anggara, W. N. Delgass, J. T. Miller, F. H. Ribeiro, R. Gounder and W. F. Schneider, *J. Am. Chem. Soc.*, 2016, **138**, 6028–6048.

124 C. Paolucci, I. Khurana, A. A. Parekh, S. Li, A. J. Shih, H. Li, J. R. Di Iorio, J. D. Albarracin-Caballero, A. Yezerets, J. T. Miller, W. N. Delgass, F. H. Ribeiro, W. F. Schneider and R. Gounder, *Science*, 2017, **357**, 898–903.

125 M.-L. Tsai, R. G. Hadt, P. Vanelderen, B. F. Sels, R. A. Schoonheydt and E. I. Solomon, *J. Am. Chem. Soc.*, 2014, **136**, 3522–3529.

126 P. J. Smeets, R. G. Hadt, J. S. Woertink, P. Vanelderen, R. A. Schoonheydt, B. F. Sels and E. I. Solomon, *J. Am. Chem. Soc.*, 2010, **132**, 14736–14738.

127 M. H. Mahyuddin, T. Tanaka, A. Staykov, Y. Shiota and K. Yoshizawa, *Inorg. Chem.*, 2018, **57**, 10146–10152.

128 G. Li, P. Vassilev, M. Sanchez-Sanchez, J. A. Lercher, E. J. M. Hensen and E. A. Pidko, *J. Catal.*, 2016, **338**, 305–312.

129 Z.-J. Zhao, A. Kulkarni, L. Vilella, J. K. Nørskov and F. Studt, *ACS Catal.*, 2016, **6**, 3760–3766.

130 K. D. Vogiatzis, G. Li, E. J. M. Hensen, L. Gagliardi and E. A. Pidko, *J. Phys. Chem. C*, 2017, **121**, 22295–22302.

131 G. S. Hammond, *J. Am. Chem. Soc.*, 1955, **77**, 334–338.

132 J. E. Leffler, *Science*, 1953, **117**, 340–341.

133 D. Schröder, S. Shaik and H. Schwarz, *Acc. Chem. Res.*, 2000, **33**, 139–145.

134 H. Schwarz, *Catal. Sci. Technol.*, 2017, **7**, 4302–4314.

135 J. L. DuBois, P. Mukherjee, A. M. Collier, J. M. Mayer, E. I. Solomon, B. Hedman, T. D. P. Stack and K. O. Hodgson, *J. Am. Chem. Soc.*, 1997, **119**, 8578–8579.

136 M. J. Henson, P. Mukherjee, D. E. Root, T. D. P. Stack and E. I. Solomon, *J. Am. Chem. Soc.*, 1999, **121**, 10332–10345.

137 C. M. Zicovich-Wilson, A. Corma and P. Viruela, *J. Phys. Chem.*, 1994, **98**, 10863–10870.

138 A. Corma, G. Hermenegildo, G. Sastre and P. M. Viruela, *J. Phys. Chem. B*, 1997, **101**, 4575–4582.

139 N. Dietl, M. Schlangen and H. Schwarz, *Angew. Chem., Int. Ed.*, 2012, **51**, 5544–5555.

140 C. Liu, G. Li and E. A. Pidko, *Small Methods*, 2018, **2**, 1800266.

141 A. A. Latimer, A. R. Kulkarni, H. Aljama, J. H. Montoya, J. S. Yoo, C. Tsai, F. Abild-Pedersen, F. Studt and J. K. Nørskov, *Nat. Mater.*, 2017, **16**, 225–229.

142 G. Wang, L. Huang, W. Chen, J. Zhou and A. Zheng, *Phys. Chem. Chem. Phys.*, 2018, **20**, 26522–26531.

143 M. F. Fellah and I. Onal, *J. Phys. Chem. C*, 2010, **114**, 3042–3051.

144 R. A. Periana, *Science*, 2017, **358**, eaan5970.

145 J. A. Labinger, *Science*, 2018, **359**, eaar4968.

146 D. Kaucký, J. Dědeček and B. Wichterlová, *Microporous Mesoporous Mater.*, 1999, **31**, 75–87.

147 K. Nakamura, A. Okuda, K. Ohta, H. Matsubara, K. Okumura, K. Yamamoto, R. Itagaki, S. Suganuma, E. Tsuji and N. Katada, *ChemCatChem*, 2018, **10**, 3806–3812.

This journal is © The Royal Society of Chemistry 2019

Catal. Sci. Technol., 2019, **9**, 1744–1768 | **1767**

148 S. Itoh, H. Bandoh, M. Nakagawa, S. Nagatomo, T. Kitagawa, K. D. Karlin and S. Fukuzumi, *J. Am. Chem. Soc.*, 2001, **123**, 11168–11178.

149 M. H. Mahyuddin and K. Yoshizawa, *Catal. Sci. Technol.*, 2018, **8**, 5875–5885.

150 E. A. Pidko, *ACS Catal.*, 2017, 7, 4230–4234.

151 A. A. Latimer, A. Kakekhani, A. R. Kulkarni and J. K. Nørskov, *ACS Catal.*, 2018, **8**, 6894–6907.

152 T. Ikuno, J. Zheng, A. Vjunov, M. Sanchez-Sanchez, M. A. Ortuño, D. R. Pahls, J. L. Fulton, D. M. Camaioni, Z. Li, D. Ray, B. L. Mehdi, N. D. Browning, O. K. Farha, J. T. Hupp, C. J. Cramer, L. Gagliardi and J. A. Lercher, *J. Am. Chem. Soc.*, 2017, **139**, 10294–10301.

153 J. Baek, B. Rungtaweevoranit, X. Pei, M. Park, S. C. Fakra, Y.-S. Liu, R. Matheu, S. A. Alshmimri, S. Alshehri, C. A. Trickett, G. A. Somorjai and O. M. Yaghi, *J. Am. Chem. Soc.*, 2018, **140**, 18208–18216.

154 D. Y. Osadchii, A. I. Olivos-Suarez, Á. Szécsényi, G. Li, M. A. Nasalevich, I. A. Dugulan, P. S. Crespo, E. J. M. Hensen, S. L. Veber, M. V. Fedin, G. Sankar, E. A. Pidko and J. Gascon, *ACS Catal.*, 2018, **8**, 5542–5548.

155 S. M. Cohen, *Chem. Rev.*, 2012, **112**, 970–1000.

156 P. Hohenberg and W. Kohn, *Phys. Rev.*, 1964, **136**, B864–B871.

157 W. Kohn and L. J. Sham, *Phys. Rev.*, 1965, **140**, A1133–A1138.

158 G. Kresse and J. Furthmüller, *Comput. Mater. Sci.*, 1996, **6**, 15–50.

159 G. Kresse and J. Furthmüller, *Phys. Rev. B: Condens. Matter Mater. Phys.*, 1996, **54**, 11169–11186.

160 P. E. Blöchl, *Phys. Rev. B: Condens. Matter Mater. Phys.*, 1994, **50**, 17953–17979.

161 G. Kresse and D. Joubert, *Phys. Rev. B: Condens. Matter Mater. Phys.*, 1999, **59**, 1758–1775.

162 J. P. Perdew, K. Burke and M. Ernzerhof, *Phys. Rev. Lett.*, 1996, **77**, 3865–3868.

163 J. Sun, B. Xiao and A. Ruzsinszky, *J. Chem. Phys.*, 2012, **137**, 51101.

164 J. Sun, R. Haunschild, B. Xiao, I. W. Bulik, G. E. Scuseria and J. P. Perdew, *J. Chem. Phys.*, 2013, **138**, 44113.

165 S. Grimme, *J. Comput. Chem.*, 2006, **27**, 1787–1799.

166 G. Henkelman, B. P. Uberuaga and H. Jónsson, *J. Chem. Phys.*, 2000, **113**, 9901–9904.

167 S. Smidstrup, A. Pedersen, K. Stokbro and H. Jónsson, *J. Chem. Phys.*, 2014, **140**, 214106.

168 G. Henkelman, A. Arnaldsson and H. Jónsson, *Comput. Mater. Sci.*, 2006, **36**, 354–360.

169 K. Momma and F. Izumi, *J. Appl. Crystallogr.*, 2011, **44**, 1272–1276.

170 J. Heyd and G. E. Scuseria, *J. Chem. Phys.*, 2004, **121**, 1187–1192.

171 J. Heyd, J. E. Peralta, G. E. Scuseria and R. L. Martin, *J. Chem. Phys.*, 2005, **123**, 174101.

172 A. D. Becke, *Phys. Rev. A: At., Mol., Opt. Phys.*, 1988, **38**, 3098–3100.

173 C. Lee, W. Yang and R. G. Parr, *Phys. Rev. B: Condens. Matter Mater. Phys.*, 1988, **37**, 785–789.

174 S. H. Vosko, L. Wilk and M. Nusair, *Can. J. Phys.*, 1980, **58**, 1200–1211.

175 A. J. H. Wachters, *J. Chem. Phys.*, 1970, **52**, 1033–1036.

176 P. J. Hay, *J. Chem. Phys.*, 1977, **66**, 4377–4384.

177 G. A. Andrienko, *ChemCraft Version 1.8.*, http://www.chemcraftprog.com, (accessed 9 October 2018).